Geochemistry, Geophysics, Geosystems®

Low-Temperature Thermochronologic Response to Magmatic Reheating: Insights From the Takab Metallogenic District of NW Iran, (Arabia-Eurasia Collision Zone)

Masoud Biralvand[1] [ID], **Paolo Ballato[2]** [ID], **Maria Laura Balestrieri[3]** [ID], **Mohammad Mohajjel[1]**, **Edward R. Sobel[4]** [ID], **Istvan Dunkl[5]**, **Giordano Montegrossi[3]**, **Mohammad R. Ghassemi[6,7]**, **Johannes Glodny[8]** [ID], and **Manfred R. Strecker[4]** [ID]

[1]Department of Geology, Tarbiat Modares University, Tehran, Iran, [2]Department of Science, University of Roma 3, Rome, Italy, [3]Institute of Geosciences and Georesources, National Research Council (CNR), Florence, Italy, [4]Institute of Geosciences, University of Potsdam, Potsdam, Germany, [5]Department of Sedimentology & Environmental Geology, University of Gottingen, Gottingen, Germany, [6]Research Institute for Earth Science, Geological Survey of Iran, Tehran, Iran, [7]School of Geology, College of Science, University of Tehran, Tehran, Iran, [8]GeoForschungsZentrum, GFZ Potsdam, Potsdam, Germany

Abstract The interpretation of low-temperature thermochronology (LTT) data in magmatic and metallogenic provinces requires a knowledge of the geothermal field through time. There, the challenge is differentiating rapid cooling following transient perturbations of the geotherms (reheating) from exhumational cooling induced by erosion during tectonic uplift or normal faulting. The Takab Range Complex (NW Iran) is a basement-cored range of the Arabia-Eurasia collision zone that experienced voluminous Eocene to Miocene magmatism and mineralization. Our new apatite and zircon (U-Th-Sm)/He and apatite fission track data, together with field observations, a dedicated numerical thermal model, and a re-evaluation of available geochronology data document the occurrence of a complex geological and thermal history including: (a) late Cretaceous-Paleocene exhumation possibly controlled by regional contractional deformation followed by Eocene deposition; (b) Oligocene to possibly early Miocene (29 to 22–20 Ma) exhumation of basement rocks from 13 to 8 km of depth, most likely through normal faulting during a thermal anomaly that led to migmatization and partial melting; (c) early to late Miocene (∼22–20 or earlier to 11–10 Ma) regional subsidence with deposition of an up to ∼2- to 3-km-thick Oligo-Miocene sedimentary sequence in association with the emplacement of shallow intrusions, which led to a partial to total reset of our LTT systems sometime between 18 and 13 Ma; and (e) erosional exhumation after 11–10 Ma with the development of a transpressional system and a master, right-lateral, strike slip fault (Chahartagh Fault). Our data highlights the impact of magmatic reheating on LTT ages in areas affected by intense magmatism.

1. Introduction

The advance of low-temperature thermochronology (LTT) and associated modeling techniques has significantly improved our ability to determine the timing and rates of near-surface geological processes and to document spatio-temporal patterns of erosional/tectonic exhumation (e.g., Braun et al., 2012; Gallagher, 2012; Gallagher & Parra, 2020; Ketcham, 2005; Ketcham et al., 2018; Murray et al., 2022; Willett et al., 2021). However, the interpretation of LTT data sets in regions characterized by widespread and prolonged magmatic activity, can be complicated by transient episodes of heating and cooling (i.e., reheating) that could be misinterpreted as episodes of burial and exhumation, respectively (e.g., Murray et al., 2018). Transient thermal events can be further amplified by the effect of fluids rising along faults and fracture zones or through highly permeable rocks, which can affect the heating/cooling rate of the rocks and lead to localized mineralization processes (e.g., Fu et al., 2010; Luijendijk, 2019; Sánchez et al., 2021). These complexities highlight the need to tackle the exhumation history of magmatic provinces through a multidisciplinary strategy integrating different data sets.

The Takab Range Complex (TRC) is a basement-cored range of the Arabia-Eurasia collision zone in the interior of the Iranian Plateau (IP) (Figure 1) and represents one of the few localities in Iran where the Neoproterozoic crystalline basement is exposed at the surface (e.g., Hajialioghli et al., 2007; Figure 2). The range was exhumed from middle crustal levels, but the processes and geodynamics associated with this exhumation are controversial. These mechanisms include tectonic denudation through normal faulting during extension (Shafaii Moghadam
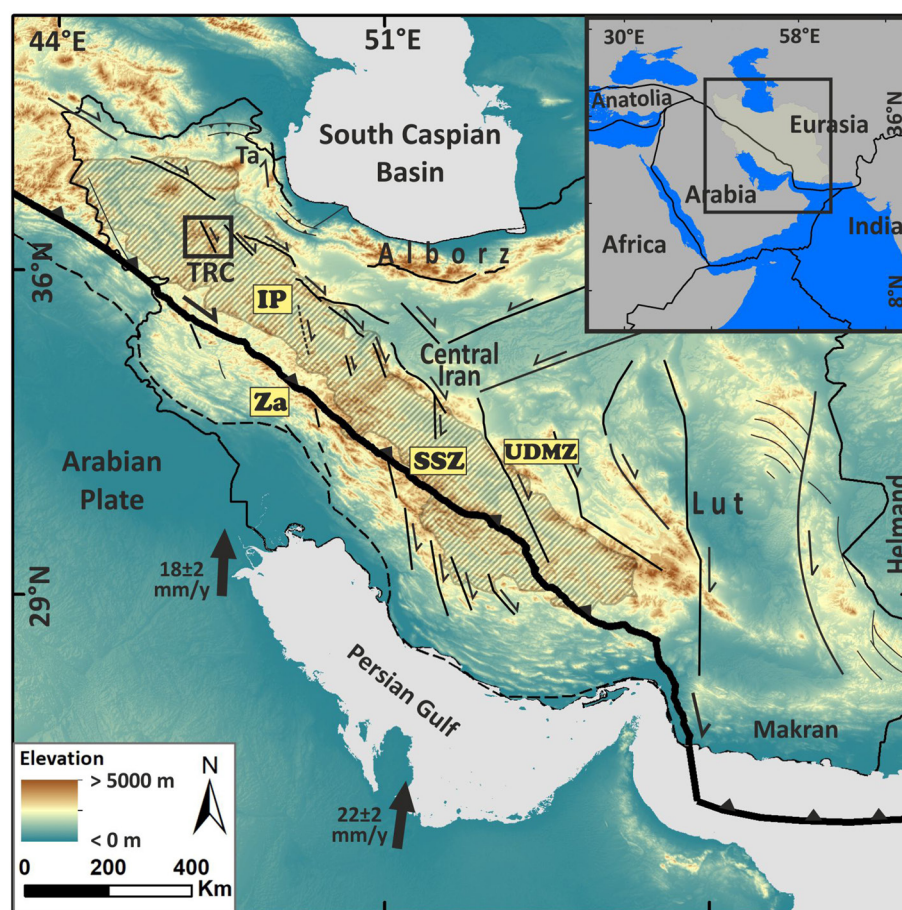
Figure 1. Digital Elevation Model of Iran, showing plate convergence vectors between Arabia and Eurasia (Vernant et al., 2004), the extent of the Iran Plateau (hatched area, Ballato et al., 2017), the approximate location of the suture between Arabia and Eurasia (black thick line) and our study area (black rectangle). Abbreviations: TRC, Takab Range Complex; IP, Iranian Plateau; SSZ, Sanandaj-Sirjan Zone; UDMZ, Urumieh-Dokhtar Magmatic Zone; Za, Zagros mountains; and Ta, Talesh mountains.

et al., 2016, 2017; Stockli et al., 2004) versus erosional unroofing during thrusting and compression (Hajialioghli et al., 2011; Moazzen et al., 2013; Saki et al., 2012). The TRC was also affected by a rather continuous magmatism lasting ~40 Myr, from the early Eocene to the late Miocene (Figure 2b and references therein), in association with mineralization processes (Table 1 and references therein). Currently, the Takab metallogenic district is one of the most exploited areas of Iran with different types of epithermal Au, Pb, Fe, Zn, As, and Sb ore deposits among others (Figure 2 and Table 1). Thus, the TRC represents an ideal setting for investigating the roles of magmatism, mineralization, and tectonics in controlling the cooling history in a metallogenic district, as recorded by LTT data. Moreover, new thermochronologic data can provide insights into the regional tectonic history that led to the local exposure of basement rocks.

To tackle these issues, we collected new field-based (structural and stratigraphic) data, compiled published geochronology and mineralization ages (zircon U-Pb, Rb-Sr, Ar-Ar, and K-Ar on K-bearing minerals and rocks), re-evaluated available geologic maps based on the new geochronological ages and our field observations, performed Apatite Fission Track (AFT) and (U-Th-Sm)/He dating on apatite (AHe) and zircon (ZHe), and designed a numerical thermal model to quantify the heat distribution through conduction and convection (i.e., magnitude and duration of reheating) in the upper crust following the emplacement of a relatively shallow intrusive body. The results of the thermal model were then imported in HeFTy (Ketcham, 2005) to test the general effect of reheating on LTT systems (ZHe, AFT, and AHe). Overall, this study allows: (a) exploring the effect of transient heating/cooling on a LTT data set and (b) unraveling the complex Cenozoic geological history of the
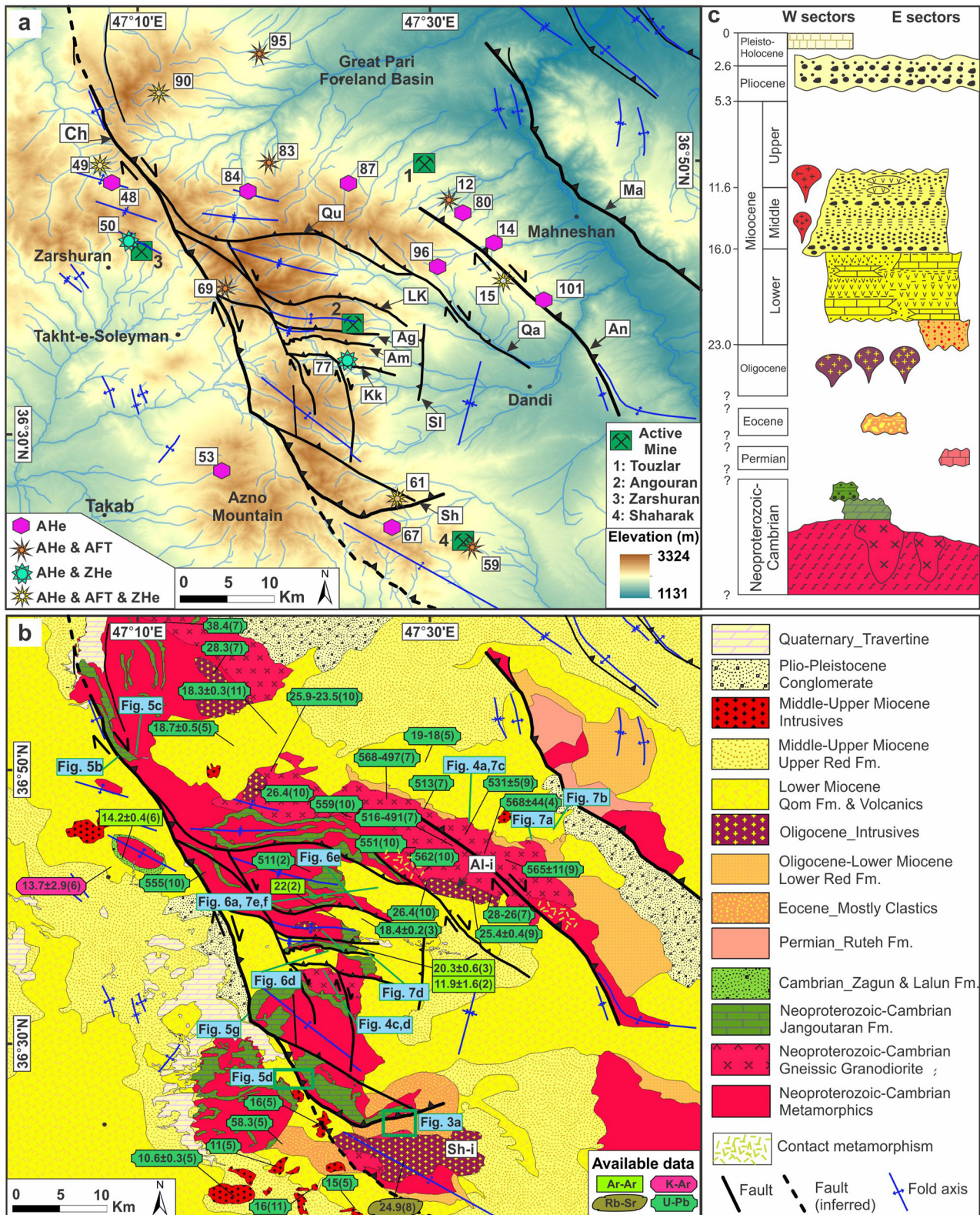
Figure 2.

Table 1

Summary of Major Regional Mineralization Events Based on (a): Heidari et al. (2015), (b): Daliran et al. (2013), (c): Gilg et al. (2006), (d): Mehrabi et al. (1999), and (e): Sepahi et al. (2020)

Mine	Type of mineralization	Host rock type and age	Age of associated volcanism	Age of mineralization	Estimated max temperature	Estimated depth
Touzlar(a)	Epithermal stratovolcano hosted mineralization	Early middle Miocene pyroclastics and lavas	19.3–18.1 Ma[a]	19.3–18.1 Ma[a]	211–310°C[f]	NA
Angouran(b and c)	Hypogene zinc sulfide-zinc carbonate (b)	Basement (mostly schist)	18.4[a]–11.9[b] Ma	Most likely during volcanism (18.4–11.9 Ma).Certainly >10 ± 1 Ma[b]	>155°C[g]	NA
	Sulfide and carbonate ore (c)	Carbonate (marble)	–	The host non-mineralized rocks has an Ar-Ar age of 21–20 Ma, so mineralization must be <20 Ma[c]	<180°C[g]	NA
Zarshouran(d)	Epithermal carbonate hosted mineralization	Basement (pre-Cambrian dolomite)	16.2 ± 0.3–11.1 ± 03 Ma[b,d]	Age favored by authors:∼14.3 ± 04 Ma[g],partial reset of the K-Ar system in the host, non-mineralized rocks at 24–27, 21–20 and 17–18 Ma	243 ± 59°C[h]	3.8 ± 1.8 Km[h]
Shaharak (e)	Iron mineralization (magnetite skarn)	Oligocene granitoide	∼25 Ma[e]	∼25 Ma[e]	∼250°C	–

Note. Note that Touzlar, Angouran, and Zarshouran mines are in the central sectors of the TRC from ENE to WSW (Figure 2) and are associated with volcanic activity, while the Shaharak mine is located at the southern TRC margin and is associated with intrusive activity.
[a]Zircon U/Pb. [b]Whole rock Ar/Ar. [c]Mica Ar/Ar. [d]Whole rock K/Ar. [e]Whole rock Rb-Sr. [f]Homogenization temperatures of the liquid rich fluid inclusion from mineralized quartz veins. [g]Homogenization temperatures of fluid inclusion from sphalerite. [h]Combination of carbonic and aqueous inclusion data with stratigraphic and mineral stability data.

TRC, which involves episodes of contractional deformation, sedimentation, magmatism, and cooling related to erosional exhumation, (possibly) tectonic denudation, and thermal perturbations.

2. Geological Setting

2.1. Regional Tectonic Setting

The Arabia-Eurasia continental collision has led to the development of a large deformation zone that extends from the Caucasus to the Persian Gulf and from eastern Turkey to western Afghanistan (e.g., Hatzfeld & Molnar, 2010 and reference therein). Although the timing of collision in NW and central Iran is still debated, an increasing number of studies suggest that it must have occurred sometime between the latest Eocene (∼35 Ma; e.g., Allen & Armstrong, 2008; Ballato et al., 2011; Darin & Umhoefer, 2022; Mouthereau et al., 2012) and the early (∼27 Ma; Koshnaw et al., 2019; McQuarrie & van Hinsbergen, 2013: Pirouz et al., 2017) to late Oligocene (Cai et al., 2021; Gholami Zadeh et al., 2017). The collision zone includes prominent mountain chains (e.g., Zagros, Alborz, Kopeh-Dagh, and Talesh Mountains) and large N-S to NW-SE and NE-SW oriented strike-slip fault systems that bound relatively rigid crustal blocks (Central Iran, Lut and Helmand blocks, south Caspian basin, and IP, Figure 1; e.g., Vernant et al., 2004). Within these blocks, the IP is an elevated morphotectonic province mostly built onto the NW-SE striking Sanandaj-Sirjan Zone (SSZ) and Urumieh-Dokhtar Magmatic Zone (UDMZ,

Figure 2. (a) Digital Elevation Model of the Takab Range Complex (TRC) with sample position, analysis type, and main geological structures. (b) Geological map of the TRC showing available geochronological ages. (c) Simplified stratigraphy of the TRC; the size of the Mio-Holocene time scale is proportional to time, which is expressed in Myr. ^{40}Ar-^{39}Ar ages are from, (2) Daliran et al. (2013), (3) Gilg et al. (2006), and (6) Mehrabi et al. (1999); K-Ar ages are from (6) Mehrabi et al. (1999); Rb-Sr ages are from Sepahi et al., 2020; Zircon U-Pb ages are from (2) Daliran et al. (2013), (4) Hassanzadeh et al. (2008), (5) Heidari (2013), and (7) Shafaii Moghadam et al. (2016). (8) Sepahi et al., 2020, (9) Honarmand et al., 2018, (10) Shafaii Moghadam et al. (2017), and (11) Azizi et al. (2021). Abbreviations: Am, Amirabad Fault; An, Angouran Fault; Ch, Chahartagh Fault; Kk, Kaka Fault; Lk, Lalekan Fault; Ma, Mahneshan Fault; Qu, Qozlu Fault; Qa, Qarenaz Fault; Ag, Angouran Mine Fault; Sh, Shahrak Fault; Sl, Sheikhlar Fault; Ts, Takht-e Soleyman Fault; Al-i, Almalou granite (∼25 Ma); and Sh-i, Shahrak intrusive body (∼25 Ma, but possibly assembled during earlier intrusions).

Figure 1; Ballato et al., 2017). Plateau uplift occurred sometime after the ∼17 Ma regional marine regression (top of the Qom Formation e.g., Ballato et al., 2017). The NW sectors of the plateau are characterized by a contractional basin-and-range landscape that started developing in the middle to late Miocene in response to collisional shortening and thickening processes (Ballato et al., 2017; François et al., 2014; Mouthereau et al., 2012; Paknia, Ballato, Heidarzadeh, Cifelli, Hassanzadeh, et al., 2021). The TRC constitutes a major mountain range within the plateau interior at the boundary between the metamorphic SSZ and the UDMZ (e.g., Stöcklin, 1968; Figure 1). The TRC presents a few peculiarities such as the exposure of a metamorphic basement and the occurrence of Eocene to late Miocene magmatism and associated mineralizations (Figure 2 and Table 1). The Eocene magmatism has a magmatic arc signature whereas the Miocene magmatism is interpreted as syn-collisional, most likely resulting from partial melting of the Eurasian mantle lithosphere metasomatized by fluids from the subducted Neo-Tethys oceanic lithosphere (e.g., Azizi et al., 2021; Kaislaniemi et al., 2014; Rabiee et al., 2020, 2022). Syn-collisional magmatism is spatially and temporally scattered across the entire Arabia-Eurasia collision zone and has been interpreted to occur in areas of variable lithospheric thickness in response to small-scale convection at the lithosphere-asthenosphere boundary (Kaislaniemi et al., 2014).

2.2. Tectono-Stratigraphic Setting and Late Cenozoic Magmatic History of the TRC

The TRC consists of upper Neoproterozoic crystalline basement rocks (gneisses, granulites, amphibolites, schists, marbles, meta-ultramafic, and intrusive rocks) with metamorphic conditions ranging from greenschist to granulite facies that were assembled during the Pan-African Orogeny (zircons U-Pb ages are mostly 550–500 Ma, Figure 2; e.g., Hassanzadeh et al., 2008; Moazzen et al., 2009; Shafaii Moghadam et al., 2016, 2017). From the Mesozoic, the TRC became the upper plate of the Neo-Tethys subduction system and was affected by multiple episodes of arc magmatism (e.g., Hassanzadeh et al., 2008). The Eocene flare up is the most voluminous magmatic event recorded in Iran (e.g., Verdel et al., 2011) and was followed by an Oligocene to possibly early Miocene (∼29–22 Ma) phase of intrusive activity associated with the emplacement of granitoids (mainly granodiorite) and the development of migmatites (Figure 2, Hajialioghli et al., 2011; Honarmand et al., 2018; Moazzen et al., 2013; Sepahi et al., 2020; Shafaii Moghadam et al., 2016, 2017). The geodynamic setting that caused migmatization, however, is not clear and has been linked either to core complex formation during upper plate (intra-arc) extension (Shafaii Moghadam et al., 2016, 2017; Stockli et al., 2004) or partial melting of a thickened lithosphere during collisional deformation (Hajialioghli et al., 2011; Honarmand et al., 2018). Partial melting may have been facilitated by the occurrence of a lithospheric scale, inherited boundary such as a slab tear that could have focused asthenospheric upwelling (Rabiee et al., 2020, 2022).

The uppermost section of the crystalline basement consists of paragneiss grading upward into a few-hundred meters thick package of dolomites and crystalline dolomitic limestone (Jangoutaran Formation; Figure 2b). The basement is either covered by lower Cambrian marine to continental clastics and carbonates, Eocene clastics (coeval with the volcaniclastic deposits of the Karaj Formation; e.g., Verdel et al., 2011), Oligo-Miocene continental conglomerates of the Lower Red Formation (LRF), lower Miocene shallow-water marine sediments (mostly limestone; Qom Formation; e.g., Mohammadi et al., 2015) interfingered with volcanics (andesites, rhyolites, and dacites; Heidari et al., 2015), or middle to upper Miocene terrestrial clastic deposits of the Upper Red Formation (URF, e.g., Ballato et al., 2017; Figure 2c).

In the eastern TRC, the Miocene volcanics have an age ranging from 19.3 to 18.1 Ma and have been interpreted to represent a stratovolcano that was eroded during the late Cenozoic compressional deformation (Table 1, Azizi et al., 2021; Heidari et al., 2015). These volcanics are interlayered with the shallow-water marine sediments of the Qom Formation and are superseded by the middle to upper Miocene red clastics of the Upper Red Formation (URF) (Figure 2). The contact between the lower Miocene volcanic/marine rocks and the basement along the eastern side of the TRC has been described either as stratigraphic (Babakhani & Ghalamghash, 1998; Fonoudi & Hariri, 2000; Lotfi, 2001) or tectonic such as a detachment fault that accommodated intra-arc extension before the onset of Miocene contractional deformation (Hassanzadeh et al., 2008; Stockli et al., 2004).

To the northeast, the TRC is overlain by Mio-Pliocene sediments and volcanics (Figure 2). There, the clastic URF was deposited between ∼17 and 10.7 Ma, most likely in a foreland basin setting as suggested by a north-eastward wedging geometry of the strata (Ballato et al., 2017). In the central sectors of the TRC, the basement is also covered by ∼18.4- to 12-Myr-old volcanics (Table 1, Daliran et al., 2013) while the URF is virtually absent either because it was eroded or not deposited (Figure 2). These sectors (central TRC) include steeply dipping faults of unknown kinematics and a few south-west to south verging thrust faults (Figure 2). Although the kinematic

history and the displacement of these faults is undetermined, they have been interpreted to play an important role during mineralization processes (Daliran et al., 2013; Gilg et al., 2006; Mehrabi et al., 1999).

In the western sectors of the TRC, basement rocks are juxtaposed with Miocene volcanic, marine, and terrestrial deposits by the NNW-SSE-trending, E-dipping, reverse Chahartagh Fault. Although this structure represents a prominent magnetic lineament (Teknik & Ghods, 2017), its long-term kinematic history is poorly understood. Specifically, it is not clear whether it played a major role in uplifting basement rocks during collisional deformation (Babakhani & Ghalamghash, 1998) or it mostly accommodated right-lateral displacement (~15 km from the late Miocene to the Pliocene, Allen et al., 2011). In the western TRC, the middle to upper Miocene volcanic rocks appears to be younger than those deposited along the eastern TRC flank (Figure 2b; Table 1, Mehrabi et al., 1999). These volcanics locally overlain the URF (Mehrabi et al., 1999) or intrude it as documented by an ~11-Myr-old dacitic dome (Figure 2, Heidari, 2013). Finally, polygenic conglomerates of supposed Plio-Pleistocene age, were deposited along the margins of the TRC (Babakhani & Ghalamghash, 1998), while Quaternary travertines developed in the western sectors of the study in association with ongoing hydrothermal activity (Figure 2, Roshanak et al., 2018).

2.3. Late Cenozoic Mineralization History of the TRC

The TRC represents one of the most important mining districts of NW Iran and hosts significant epithermal mineralizations (mostly Au-Cu-Zn-Fe; Table 1 and references therein). This is thought to be related to the occurrence of specific conditions including a shallow metamorphic basement, a source of heat with metals and mineralizing hydrothermal fluids, brecciated and fractured lithologies representing fluid flow pathways in contact with reactive host rocks and domal structures such as anticlines intersected by major faults and fracture systems (e.g., Daeijavad et al., 2020 and references therein). In the hanging-wall of the Chahartagh Fault, mineralization occurred mainly in the Precambrian basement whereas in its footwall (western side of the TRC), the majority of the mineralizations are observed in Cambrian strata, Oligocene intrusives and Miocene carbonates and volcanics (Figure 2). Mineralization ages range from 20 to 12 Ma (Table 1). Temperature and pressure estimates indicate that the Miocene mineralizations occurred within temperature windows ranging from 155°C to 310°C and depths <~5 km (Table 1). These observations indicate that the geothermal gradient in the TRC must have been rather high and most likely highly variable in space and time.

## 3. Field Observations

3.1. Cenozoic Stratigraphy

Stratigraphic contacts between the crystalline basement and sedimentary units provide constraints on the timing of basement exposure and exhumation. In the following, we report our field observations relative to two Cenozoic sedimentary units that overlay basement rocks that are Eocene and Oligo-Miocene in age, respectively.

3.1.1. The Eocene Depositional Cycle

During the Eocene, the upper Eurasian plate experienced widespread magmatism and subsidence (magmatic flare up, Verdel et al., 2011; see also Boutoux et al. (2021) and reference therein for a recent review). Volcanic and volcaniclastic rocks were deposited virtually everywhere on the upper Eurasian plate, mostly in deep to shallow marine basins. In the TRC, supposed Eocene clastics can be observed only along its southern margin, in the footwall of the Shahrak Fault where they cover the crystalline basement (Figures 2b and 3). These strata consist of few-meters-thick breccia lenses containing basement and Meso-Paleozoic sedimentary blocks (Figure 3d) and laminated/rippled sandstones and mudstones representing turbidite deposits (Figure 3e). According to available geologic maps, these Eocene clastics are equivalent of the volcano-sedimentary, lower to upper Eocene, Karaj Formation, which is widely exposed in north and central Iran (Figure 2b; e.g., Verdel et al., 2011). Although the tectono-stratigraphic significance of the Eocene clastics of the TRC has not been systematically investigated yet, it marks the onset of a new cycle of subsidence and sedimentation. Such a cycle should follow or be partially coeval with a regional late Cretaceous to possibly early Paleocene compressional event (Boutoux et al., 2021 and references therein) that should have led to the exposure at the surface of the metamorphic basement.

3.1.2. The Oligo-Miocene Depositional Cycle

In the eastern sectors of the TRC the crystalline basement is covered by a discontinuous package of continental deposits, mostly conglomerates, of the LRF. In central and southern Iran, these terrestrial sediments are Oligocene
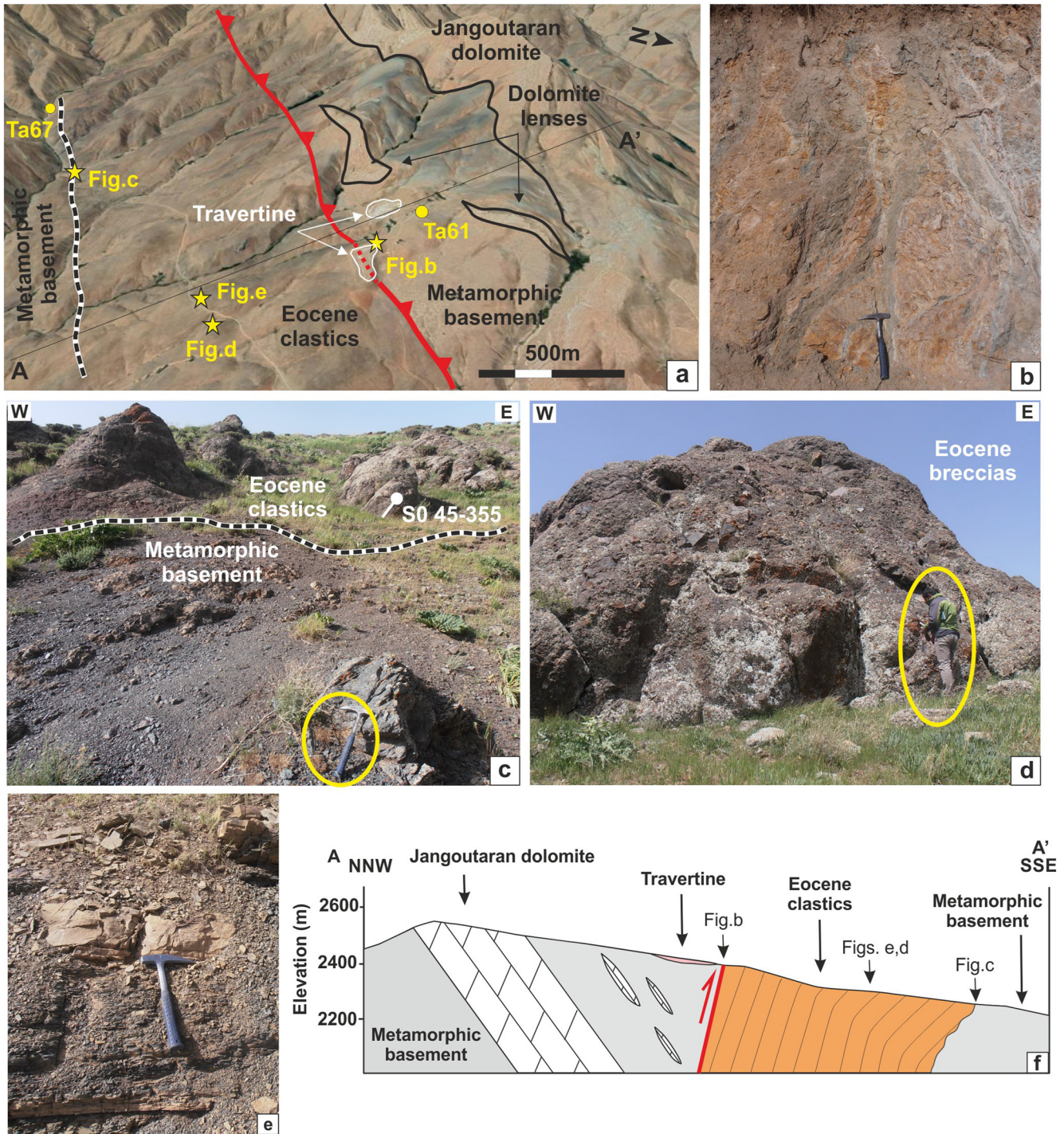
Figure 3. (a) Google Earth scene (oblique view) of the Shaharak Fault (see Figure 2 for location). (b) Close-up view of the fault zone with numerous anastomosing veins and small scales shear zone suggesting intense fluid circulation. (c) Nonconformity contact (dashed black and white line) between the metamorphic basement and Eocene clastics that include (d) breccia and (e) turbidites. (d) Schematic cross section across the Shaharak Fault. Note the presence of travertine deposits originated from springs in proximities of the fault zone in panels (a and d).

in age because they are stratigraphically underneath the well dated marine deposits of the Oligo-Miocene Qom Formation. Available biostratigraphic data, however, indicate that the marine transgression that led to the deposition of these marine deposits is time transgressive (Daneshian & Ramezani Dana, 2007; Mohammadi et al., 2015). For example, in southern and central Iran, it occurred in the early to late Oligocene, while in N and NW Iran

marine sedimentation started only in the early Miocene (Mohammadi et al., 2015 and references therein). This age pattern is consistent with a recent study from eastern Turkey where the deposition of the shallow-water marine deposits of the Van Formation started at ~20 Ma (early Burdigalian, Gülyüz et al., 2020). Furthermore, an early Miocene age for this transgression agrees with radiometric dating from the eastern TRC, where the marine deposits are inter-fingered with 19- to 18-Myr-old volcanics (Heidari et al., 2015). This information suggests that the base of the Qom Formation in the Takab area is most likely 20- to 19-Myr-old. This is also the age of the top of the LRF because the stratigraphic contact with the overlying Qom Formation, at least in this area, is conformable and not associated with major discontinuities. In the central and western sectors of the TRC, the LRF is absent, and the crystalline basement is extensively covered by marine sediments of the Qom Formation, lower to middle Miocene volcanics, and volcaniclastics, and middle to upper Miocene continental deposits of the URF (Figures 2 and 4 and Table 1).

The Oligo-Miocene deposits of the TRC are locally affected by minor normal faults (see details in Section 3.2.3), but most of the geological contacts between these volcano-sedimentary strata and the crystalline basement are nonconformities (Figures 2, 4, and 5a). This observation suggests that after the Eocene depositional cycle, most of the TRC crystalline basement was exposed at the surface at least from ~19 to 20 Ma. This is a minimum age because the occurrence of the unconformable LRF indicates that basement exposure may have occurred earlier than that. Finally, the occurrence of volcanic deposits within the lower Miocene marine carbonates of the Qom Formation and the middle-upper Miocene clastics of the URF suggests that volcanism in the TRC migrated westward from ~19 to 11 Ma (Table 1 and Figure 2).

3.2. Structural Observations

### 3.2.1. Compressional Structures in the Western TRC

In the north-western sectors of the TRC, the NNW-SSE striking Chahartagh Fault consists of a several tens of meters wide, sub-vertical (up to 85°) to ENE-dipping fault zone that juxtaposes basement rocks over lower Miocene volcanics (Figures 2 and 5a–5c). This area is characterized by high and rugged topography, with deformation that has also affected the footwall of the fault as documented by the occurrence of a right-stepping array of en-echelon, NW-SE striking anticlines and synclines (Figures 2 and 5a). The anticlines are cored by the crystalline basement and one of them hosts the epithermal gold mineralization of the Zarshuran mine (Figure 2 and Table 1). In the central sector of the Chahartagh Fault, however, the fault zone is less steep (~70°) and juxtaposes basement rocks over Miocene sediments and volcanics (approximately from the village of Chahartagh at 36°30′N to its southern termination; Figures 5d–5f). Along its southern sectors, the footwall of the fault includes a basement-cored range of limited topographic relief (Azno Mountain, Figure 1). There, the occurrence of dolomites of the Jangoutaran Formation on both hanging wall and footwall suggests ~700 m of vertical throw (Figures 5d–5f). Finally, along its southern termination, the Chahartagh Fault intersects a major E-W striking, N-dipping (<60°) fault (Shahrak Fault) that thrusts basement rocks onto Eocene clastics and lower Miocene marine sediments and volcanics (Figures 3a, 3b, and 3d). Considering that to the south, the Chahartagh Fault loses its geological and morphological expression (Figure 2), the Shahrak Fault may represent a horsetail termination of the Chahartagh Fault.

Overall, these observations indicate that the Chahartagh Fault accommodated limited vertical displacement (up to 700 m in its central sectors) and hence did not cause exhumation of the Neoproterozoic metamorphic basement during collisional deformation. This is consistent with our stratigraphic observations indicating the occurrence of a pre-Eocene and pre-early-Miocene stage of basement exhumation (see the previous Section 3.1). Concerning the supposed right-lateral displacement (~15 km from the late Miocene to Pliocene) accommodated by the Chahartagh Fault (or Takab Fault) described by Allen et al. (2011), our field observations do not provide quantitative evidence for such a displacement. However, the occurrence of tilted conglomerates of supposed Plio-Pleistocene age in the footwall of the fault suggests that it must have been active sometime during the last 5 Ma (Figures 2 and 5g).

3.2.2. Compressional Structures in the Central and Eastern TRC

Our field work allowed recognizing in the hanging wall of the Chahartagh Fault a system of sigmoidal thrust faults with an overall ~NW-SE orientation (Figure 2). Among these structures, the Qozlu, Lalekan, and Angouran Mine faults juxtapose basement rocks onto lower to middle Miocene volcanics and shallow-water marine sediments of the Qom Formation (Figures 2 and 6). Along their northwest termination, these faults affect only
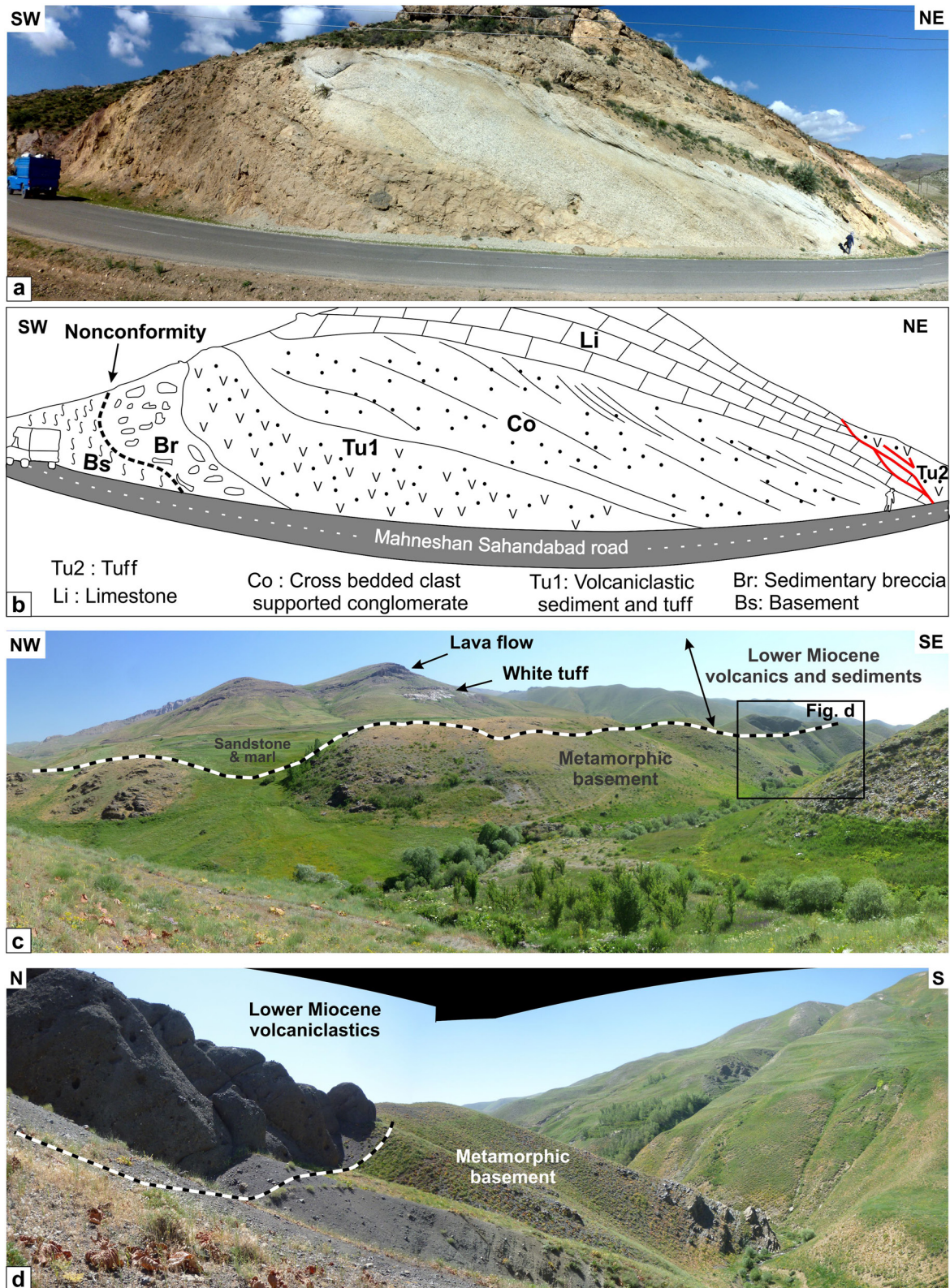
Figure 4. (a) Outcrop photograph and (b) line drawing showing the nonconformity contact (dashed black and white line) between the metamorphic basement and lower Miocene volcaniclastic and marine deposits of the Qom Formation. The normal fault at the NE corner of Figure 4a is also shown in Figure 7c. (c, d) Nonconformity contact between the metamorphic basement and lower to middle Miocene volcaniclastics deposits (see Figure 2 for location).
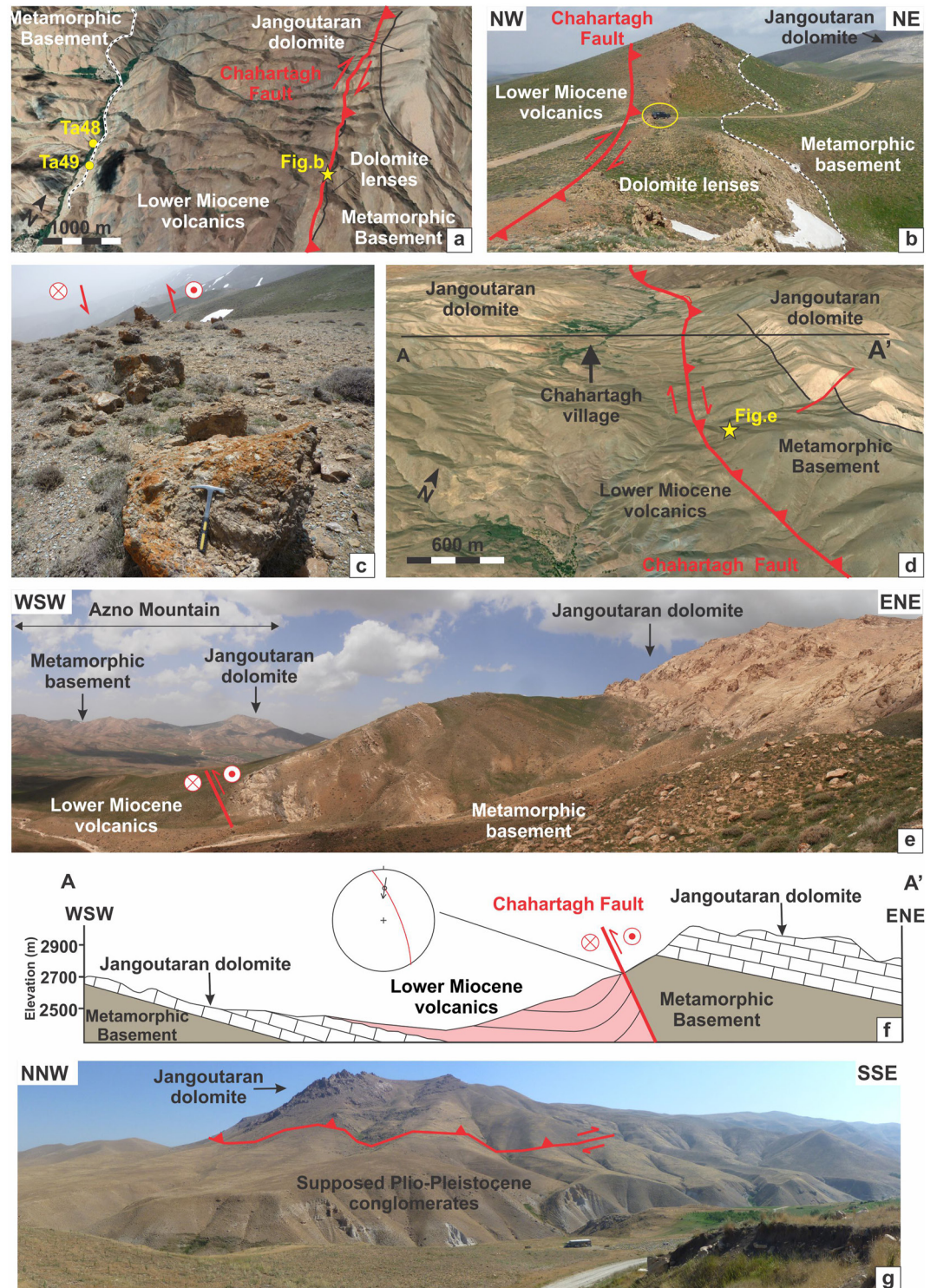
Figure 5. (a) Google Earth scene (oblique view) and field photo; (b) of the Chahartagh Fault along its northern sector; (c) of a fault strand in its hanging wall; (d) Google Earth image (oblique view); (e) field photo of the Chahartagh Fault along its central sector; (f) schematic cross section suggesting a dip-slip displacement of ~700 m; and (g) panoramic view of the Chahartagh Fault and the supposed Plio-Pleistocene conglomerates in its footwall (see Figure 2 for location). The dashed black and white line show the unconformity contact between the metamorphic basement and the lower Miocene volcanics.
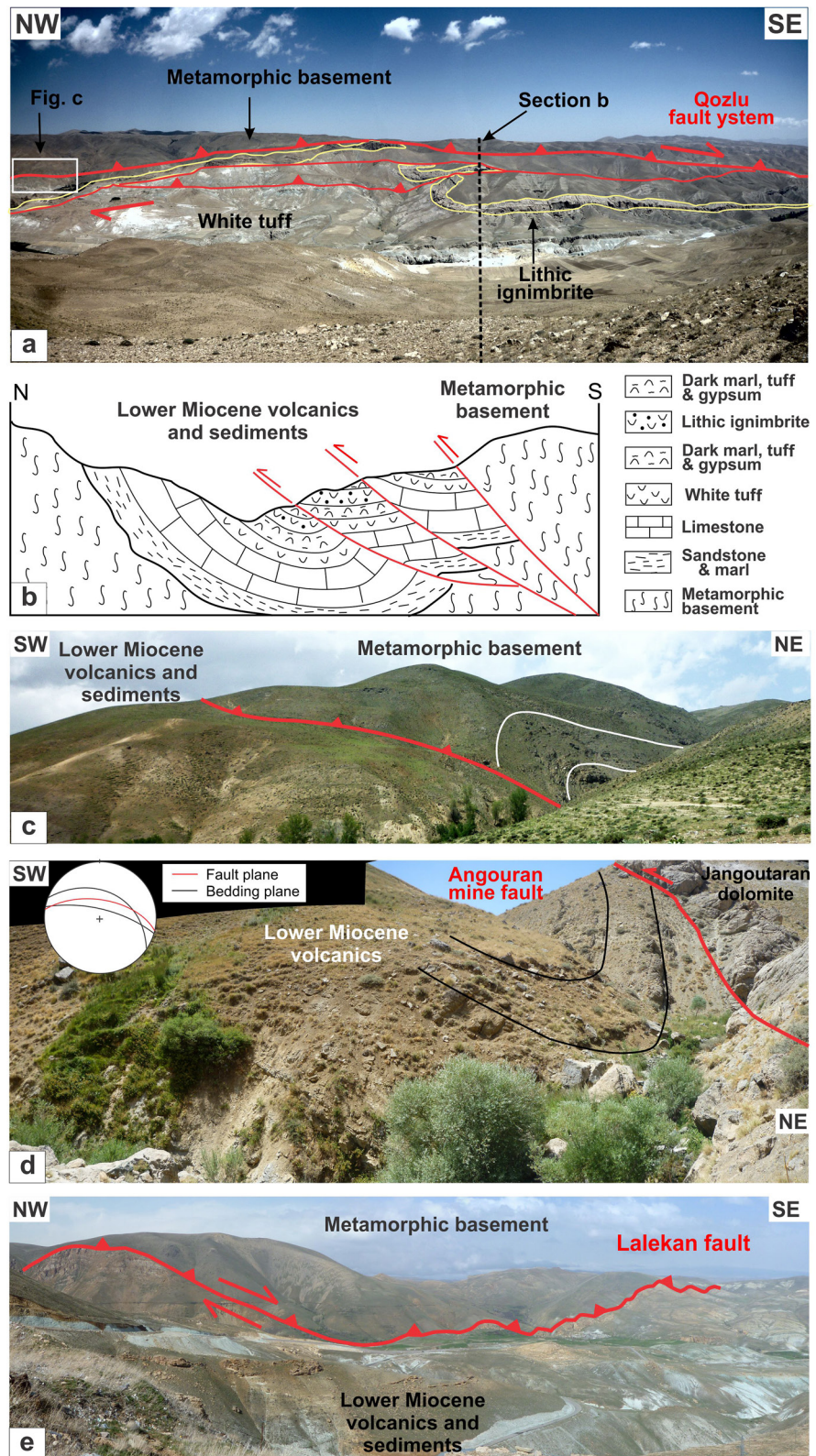
Figure 6. (a) Panoramic view and (b) schematic cross section of the southern sectors Qarenaz-Qozlu Fault along the Angouran valley showing two major footwall fault splays. Field photo of (c) the Qarenaz, (d) the Angouran mine, and (e) the Lalekan Fault with basement rocks thrusted over lower to middle Miocene volcanics and limestones (see Figure 2 for location). The yellow lines delimit a few-meter thick lithic ignimbrite, which can be followed along strike for several km.
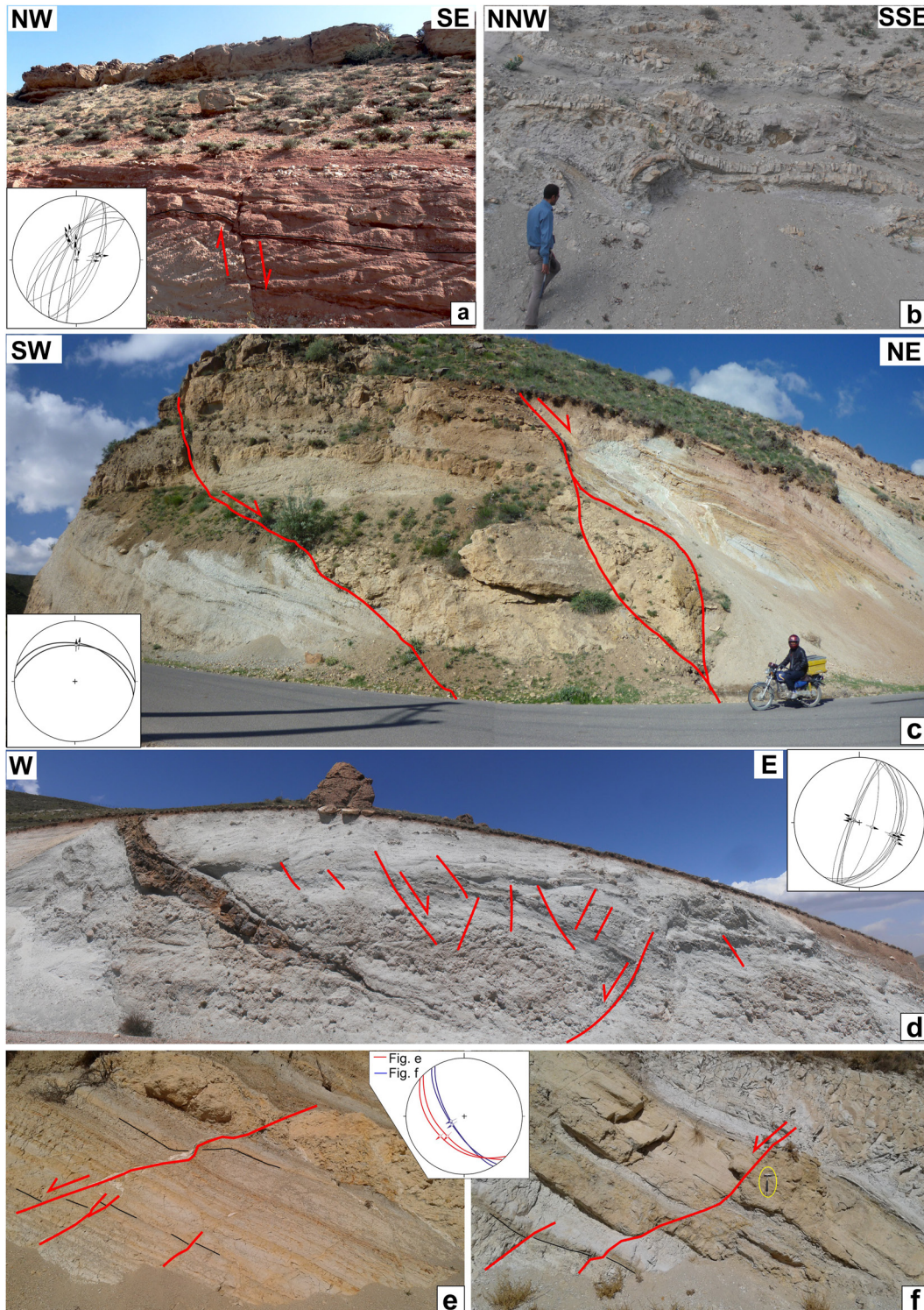
Figure 7. (a) Syn-sedimentary normal faults with a dominant dip slip (see stereoplot for orientation) in the Lower Red Formation. Note the upward decrease in fault offset and the occurrence of overlying unfaulted lower Miocene limestones of the Qom Formation. (b) Slumps in the Qom Formation along the eastern side of the Takab Range Complex. (c) Normal faults within the lower Miocene volcanics and the shallow-water marine limestones of the Qom Formation (see also Figures 4a and 4b). (d) Rhyolite pyroclastic flow cut by basalt dyke (see also Figure 4e of Daliran et al. (2013)) with synsedimentary listric normal faults. (e, f) Syn-sedimentary normal faults in the early Miocene volcanics and the shallow-water marine limestones of the Qom Formation in the Angouran valley (see Figure 2 for location). Note that all stereoplot represents major fault planes and associated dip slip slickenlines after back-tilting to the horizontal position, which is the original orientation when they formed. Note that the scale of panel (e) is approximately the same of that one of panel (f).

basement rocks, and merge with the Chahartagh Fault without continuing in its footwall. This configuration suggests a genetic link between the Chahartagh Fault and the sigmoidal thrust faults of its hanging wall. To the south, the Lalekan and Angouran Mine faults decrease progressively their displacement until their termination in the Qom and the Upper Red formations (Figure 2). The Qozlu Fault merges the Qarenaz Fault in an area characterized by a complex geometry with several splay faults that cut through the upper Cenozoic sequence (Figures 6a and 6b). Finally, the eastern sectors of the TRC are characterized by the occurrence of the NNW-SSE trending Angouran Fault that juxtapose basement rocks over Miocene Qom and URF strata (Figure 2). This structure exhibits a dip angle of ∼50° and is characterized by a right-lateral oblique thrusting kinematics. The hanging wall of the Angouran Fault contains a system of W-verging, NNW-SSE striking anticlines that bends to a ∼E-W direction around the south-eastern termination of the fault, suggesting the occurrence of right-lateral shear (Figure 2).

3.2.3. Early to Middle Miocene Normal Faults

Late Cenozoic collisional deformation in the TRC has produced a system of NNW to NW striking reverse, oblique and right-lateral strike-slip faults that have obliterated older (Eocene to middle Miocene; e.g., Morley et al., 2009; Verdel et al., 2011) extensional structures (e.g., Stockli et al., 2004; Figure 2). The main evidence documenting extensional tectonics is mostly found in the central and eastern TRC and includes syn-sedimentary, often conjugate, normal faults of limited displacement (few centimeters to few meters) affecting the lower to middle Miocene volcanics, the Qom Formation and to a lesser extent the LRF (Figure 7). These faults do not appear to affect the middle-upper Miocene URF. The few normal faults observed in the field show a variable extensional direction ranging from NW-SE to N-S and NE-SW (see stereonets of Figure 7 where fault data were back-tilted to the original sub-horizontal position). It should be also noted that within the lower Miocene volcanics and limestones exposed along the eastern sectors of the TRC, small to large-scale slumps can be observed (up to few tens of meters; Figure 7b). These structures document basin instability, most likely associated with normal faulting or by volcanic activity (Figure 7). Although the causes that led to the development of these early middle Miocene normal faults are unknown (for an overview see Paknia, Ballato, Heidarzadeh, Cifelli, Oskooi, et al., 2021 and references therein) their occurrence could have favored the rise of magma and the occurrence of widespread volcanism (e.g., Daliran et al., 2013; Heidari et al., 2015).

4. Low-Temperature Thermochronology

LTT allows to infer thermal histories of rocks from isotopic or physical properties of minerals. In this study we used (U-Th-Sm)/He on zircon and apatite and apatite fission tracks. The (U-Th-Sm)/He dating method is based on the radioactive decay of ^{235}U, ^{238}U, ^{232}Th, and ^{147}Sm by alpha (^4He nucleus) emission, and provides the cooling age of samples at nominal closure temperatures of ∼180°C (e.g., Reiners et al., 2002; Wolfe & Stockli, 2010) and ∼60°C (e.g., Farley, 2000; Wolf et al., 1996) for zircon and apatite respectively. Many factors may have an influence on the kinetics of the (U-Th-Sm)/He systems, including grain size (Reiners & Farley, 2001), radiation damage (Flowers et al., 2009; Guenthner et al., 2013), U and Th zonation (Dobson et al., 2008), and the residence time of apatites and zircons within the partial retention zone (Guenthner et al., 2013; Reiners et al., 2004). Fission tracks in minerals represent linear damage zones produced by the radioactive decay of ^{238}U (Wagner & Van den haute, 1992). Over geological time, fission tracks are fully retained in apatite at temperature below 60°C, while they are only partially retained between 60°C and 120°C (partial annealing zone, PAZ) with a mean closure temperature of 110 (±10)°C (Green & Duddy, 1989). Measurement of confined fission track lengths gives information about the way the rocks cooled through the PAZ. The annealing behavior of fission tracks varies with the apatite chemical composition. The diameter of etched spontaneous fission tracks measured parallel to apatite crystallographic c-axis (Dpar) is used as a proxy for track annealing kinetic properties (Barbarand et al., 2003; O'Sullivan & Parrish, 1995).

We collected more than 40 basement samples and a few Cambrian sedimentary rocks, Miocene volcanics and Oligocene granitoids across the entire TRC (Figure 2 and Table 2). Mineral separation was performed at the University of Potsdam (Germany) following the standard protocol including crushing, sieving, water table, magnetic, and heavy-liquid separation. About 60% of samples yielded good quality apatite and zircon grains; 26 samples were selected for AHe and ZHe dating (Figure 2), which was performed at the thermochronology laboratories of the University of Potsdam/GFZ Potsdam and Göttingen, respectively. Only nine samples were found suitable for fission track dating on apatites and the analysis was performed at the fission track laboratory of the CNR—Institute of Geosciences and Earth resources, in Italy. All LTT results are reported in the

Table 2
Summary Table Including Apatite Fission Track, Apatite, and Zircon (U-Th-Sm)/He Ages

Sample	AHe (Ma)	Mean error (My)	Aliq.	Stdv (My)	AFT (Ma)	1σ error (My)	ZHe (Ma)	Mean error (My)	Aliq.	Stdv (My)	Latitude (°)	Longitude (°)	Elevation (m)	Rock type	Unit/age
TA48	11.5	0.8	3/3	1.6	14.2	3.4					47.121	36.799	2,669	Green tuff	Early Miocene
TA49					12.7	1.1					47.123	36.798	2,676	Phyllite	Basement
TA49a1	*13.9*	*0.4*									"	"	"	"	"
TA49z1							*12.3*	*1.0*			"	"	"	"	"
TA49z3							*26.7*	*2.4*			"	"	"	"	"
TA50	8.4	1.4	3/3	0.7							47.138	36.719	2,476	Micro-conglomerate	Early Cambrian
TA50z2-z3							18.4	1.7	2/4	1.6	"	"	"	"	"
TA50z1-z4							32.5	2.7	2/4	5.6	"	"	"	"	"
TA53					29.8	4.1					47.260	36.470	2,490	Gneiss	Basement
TA53a1	*27.1*	*1.9*													
TA53a2	*43.6*	*4.0*									"	"	"	"	"
TA53a3	*61.9*	*3.6*									"	"	"	"	"
TA53a4	*43.1*	*1.7*									"	"	"	"	"
TA59	18.0	1.7	3/4	2.3	30.9	5.1					47.561	36.361	2,155	Granodiorite	Oligocene
TA61	15.2	0.5	3/3	1.2	12.4	0.7	14.1	1.1	3/3	1.5	47.472	36.413	2,429	Gneiss	Basement
TA67	20.2	1.1	3/4	4.9							47.451	36.389	2,290	Phyllite	Basement
TA69	14.5	0.5	3/3	3.3	14.7	1.4					47.259	36.670	2,700	Fine-grained granodiorite	Basement
TA77	18.7	2.8	3/3	1.0			15.5	1.5	4/4	0.5	47.400	36.586	2,849	Mica-schist	Basement
TA80	17.8	4.4	2/4	1.1							47.540	36.757	2,720	Paragneiss	Basement
TA83	13.0	1.1	3/3	3.2	12.2	1.0					47.307	36.806	3,033	Migmatite (leucosam)?	Basement
TA84	10.6	0.6	3/3	2.3							47.286	36.789	2,891	Foliated tonalite	Basement
TA87	18.6	1.6	2/4	0.1							47.398	36.791	2,693	Ortogneiss	Basement
TA90	18.5	5.6	2/4	2.3	21.3	2.1	18.6	1.4	3/3	2.1	47.213	36.892	3,496	Gneiss	Basement
TA95	22.1	1.5	4/4	3.6	25.9	3.3					47.298	36.943	2,160	Ortogneiss	Basement
TA96	18.4	0.5	3/3	2.2							47.511	36.699	2,333	Ortogneiss	Basement
TA101	15.6	1.6	2/4	0.7							47.631	36.660	2,056	Leucogranite	Basement
MH12	5.9	1.3	3/3	0.5	18.6	2.2					47.527	36.772	1,958	Green tuff	Early Miocene
MH14	22	2.6	2/3	6.1							47.574	36.721	2,084	Granite	Basement
MH15	22,4	3,4	3/4	1.9	19.7	1.8	16.5	0.8	3/3	1.4	47.594	36.682	2,260	Granite	Oligocene

Note. ZHe and AHe data are expressed as mean age. "Aliqu." represents the number of aliquots used for the mean AHe and ZHe age calculation over the total number of available aliquots (e.g., 2/4 means 2 over 4 aliquots). Single aliquots that were not included in the mean age calculation but are considered correct (i.e., do not have inclusions or major technical problem) are expressed in italics. Sample TA50 is considered to be composed of two populations with different kinetics (Table S3 in Supporting Information S1).

Supporting Information (Tables S1–S4 and Figures S1–S5 in Supporting Information S1) available here https://doi.org/10.6084/m9.figshare.21425046 and in the main text as a summary table (Table 2).

4.1. (U-Th-Sm)/He on Zircon and Apatite

Euhedral zircon and apatite crystals without apparent inclusions and other impurities were selected and packed individually in niobium (Uni Potsdam) and platinum tubes (Uni Göttingen). We analyzed three to four single-grain aliquots from each sample and used grain dimensions and number of terminations to calculate the FT correction

factor assuming a homogeneous U and Th distribution (Ketcham et al., 2011). Both zircon and apatite samples were heated with a laser to extract all He, which was purified and measured in a Quadrupole mass spectrometer. Each sample was re-extracted and analyzed to verify the complete He degassing. U, Th, and Sm were analyzed by isotope dilution. ZHe ages were calculated by the Taylor Expansion Method (Braun et al., 2012), while AHe ages were obtained using the Meesters and Dunai (2005) calculation. Additional details about the protocol followed for zircon and apatite (U-Th-Sm)/He dating can be found in Harangi et al. (2015) and Zhou et al. (2017), respectively.

4.2. Apatite Fission Tracks

Apatites were mounted in epoxy resin and ground and polished to reveal internal surface. They were etched in 5 N HNO_3 at 20°C and 20 s following the procedure describe by Barbarand et al. (2003). Samples were dated following the external detector method (Gleadow, 1981) and the Zeta calibration approach (Hurford & Green, 1983). Thermal neutron irradiation was carried out in the Lazy Susan facility (Cd ratio 6.4 for Au and 48 for Co) of the reactor Triga Mark II of the University of Pavia (Italy). Mica detectors were etched in HF (40%) for 8 min at 40°C. FT ages were calculated using a zeta value of 357.0 ± 10.2 (referred to Fish Canyon Tuff and Durango apatite standards, Hurford, 1990). A Zeiss Axioskope microscope with dry objective and 1,250x magnification was used for age counting and length measurement.

5. Results

5.1. LTT Data

The majority of the AHe single grain ages range from 3.4 to 27 Ma (57 out of 68 aliquots; Tables S1 and S2 in Supporting Information S1). Twelve aliquots were excluded from the mean age calculation because the AHe single grain ages cannot be explained by the available diffusion models. These aliquots are not considered reliable because they present very low effective Uranium content, and/or a large analytical error, and/or a small grain size (and hence large FT correction) and/or possible small solid/fluid inclusions not detected under the microscope (see Table S1 and S2 in Supporting Information S1 for details). Among these excluded aliquots, seven are older than 39.4 Ma while five are younger (see Table S1 and S2 in Supporting Information S1 for details). The mean AHe ages presented here are mostly from at least three aliquots (13 over 20 samples), while in five samples they represent the mean of two aliquots (Table 2, Figures 8 and 9). Overall, the AHe data exhibit a relatively good reproducibility with the standard deviation of the mean age that is: (a) lower than 20% of the mean age in 13 samples; (b) between 20% and 25% in five samples; and (c) >25% only in one sample. Only one sample (TA53) presents overdispersed single grain ages ranging from ~27 to 62 Ma (Table 2 and Figure 8).

The ZHe single grain ages range from 12.3 to 20.9 Ma (17 out of 20 aliquots; Table S3 in Supporting Information S1). These ages present a rather good reproducibility with less than 20% relative standard deviation of the aliquots ages in all samples. Three single grain ages, however, are slightly older than the companion aliquots (Table S3 in Supporting Information S1). These older aliquots yielded an age ranging from 26.7 to 36.2 Ma and were not used for the mean age calculation (Table 2 and Table S3 in Supporting Information S1; Figure 8). Grain size (i.e., size of the diffusion domain; Reiners et al., 2002) and accumulated radiation damage (Shuster et al., 2006) are generally considered the main causes inducing He age dispersion. This may be the case for two out of these three older aliquots (sample T50), where we observe a positive correlation between single grain age and effective uranium content (Figure S4 in Supporting Information S1).

The AFT central ages range from 30.9 to 12.2 Ma (Tables 2; Figure 8; and Table S4 in Supporting Information S1). A robust distribution ($n = 56$) of confined track lengths could be measured only in one sample (TA69, mean track length 15.0 ± 0.1 μm). Importantly, seven out of 11 samples yielded (U-Th-Sm)/He and AFT mean and central ages, respectively, overlapping within age uncertainty (Table 2; Figure 8). This overlap has specific implications that will be discussed Sections 6 and 7. Finally, sample TA61 and MH15, has an AHe mean age older than the paired mean ZHe and AFT ages (Table 2). The possible reasons for this apparently unusual behavior are discussed in Section 6.

5.2. Spatial Pattern of Thermochronological Ages

Our LTT data set presents two main trends: (a) paired thermochronometers from the same sample overlap within uncertainty in most of the samples despite 50°–65°C difference in closure temperature; and (b) samples in similar
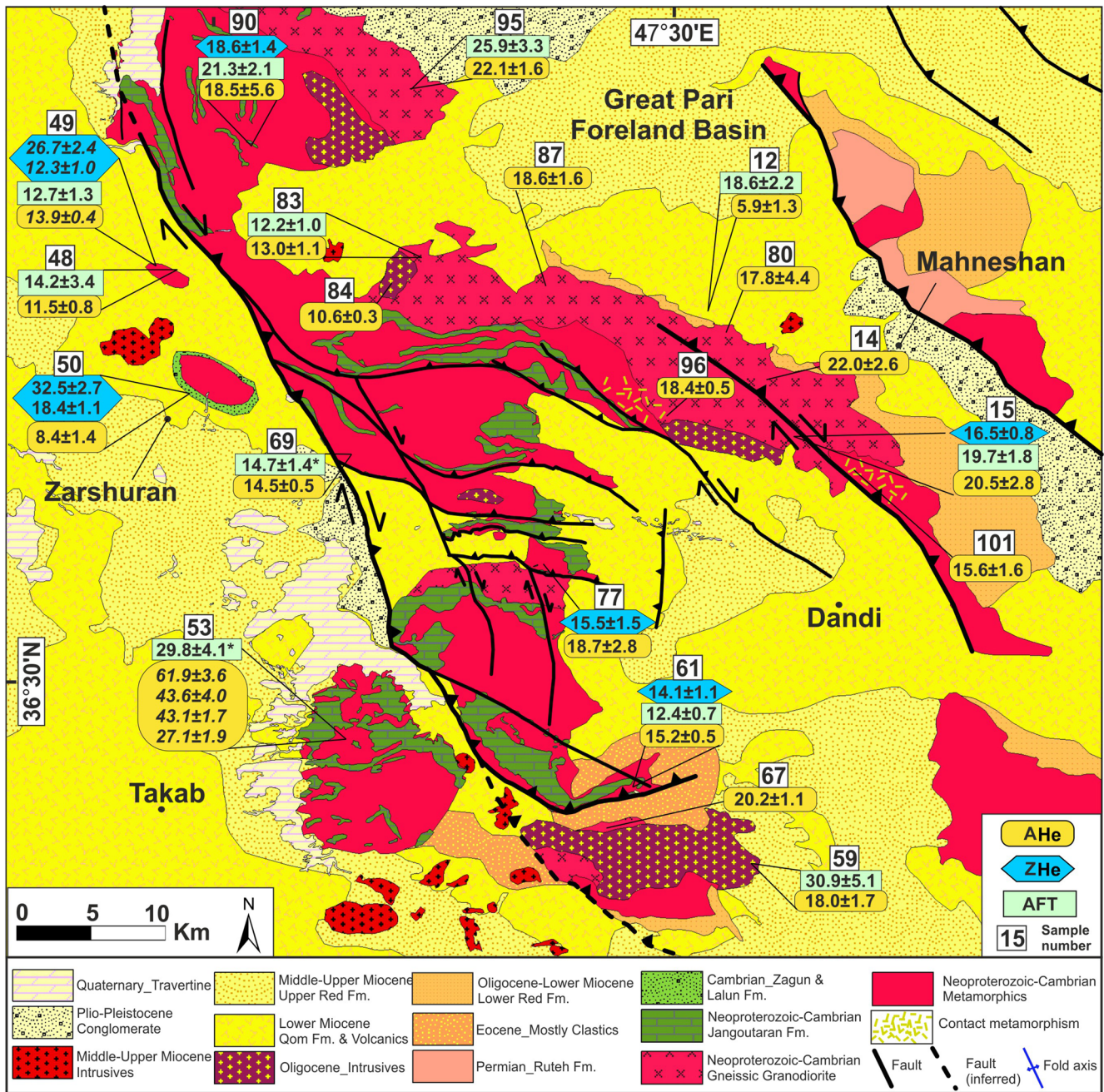
Figure 8. Geological map as in Figure 2 with samples location, Apatite fission track, zircon, and apatite (U-Th-Sm)/He cooling ages.

structural position but at different altitude have similar cooling ages despite elevation differences of up to 1.5 km (Table 2; Figures 8 and 9a). Despite the lack of a clear age-elevation relationship (Figure 9a), our thermochronological data set present a first-order spatial pattern (Figure 8). The AFT and AHe ages show a westward younging trend, which to a first approximation, seems to mimic the spatio-temporal trend in magmatism (Figure 2b). Within this trend, we differentiate four main zones that include the northern and southern margins, the eastern margin, the axial sectors, and the western margin of the TRC. 1)

1. Samples from the northern (2 samples, TA90 and TA95) and southern margins (3 samples; TA53, TA59 and TA67, footwall of the Chahartagh Fault) were collected at elevations of ~2.2–2.5 km except for sample TA90, which is the highest sample of the entire data set (~3.5 km). These samples present the oldest AFT ages ranging from 21.3 to 30.9 Ma with sample TA53 yielding an age of 29.8 ± 4.1 Ma but failing the P(χ)^2 test with a
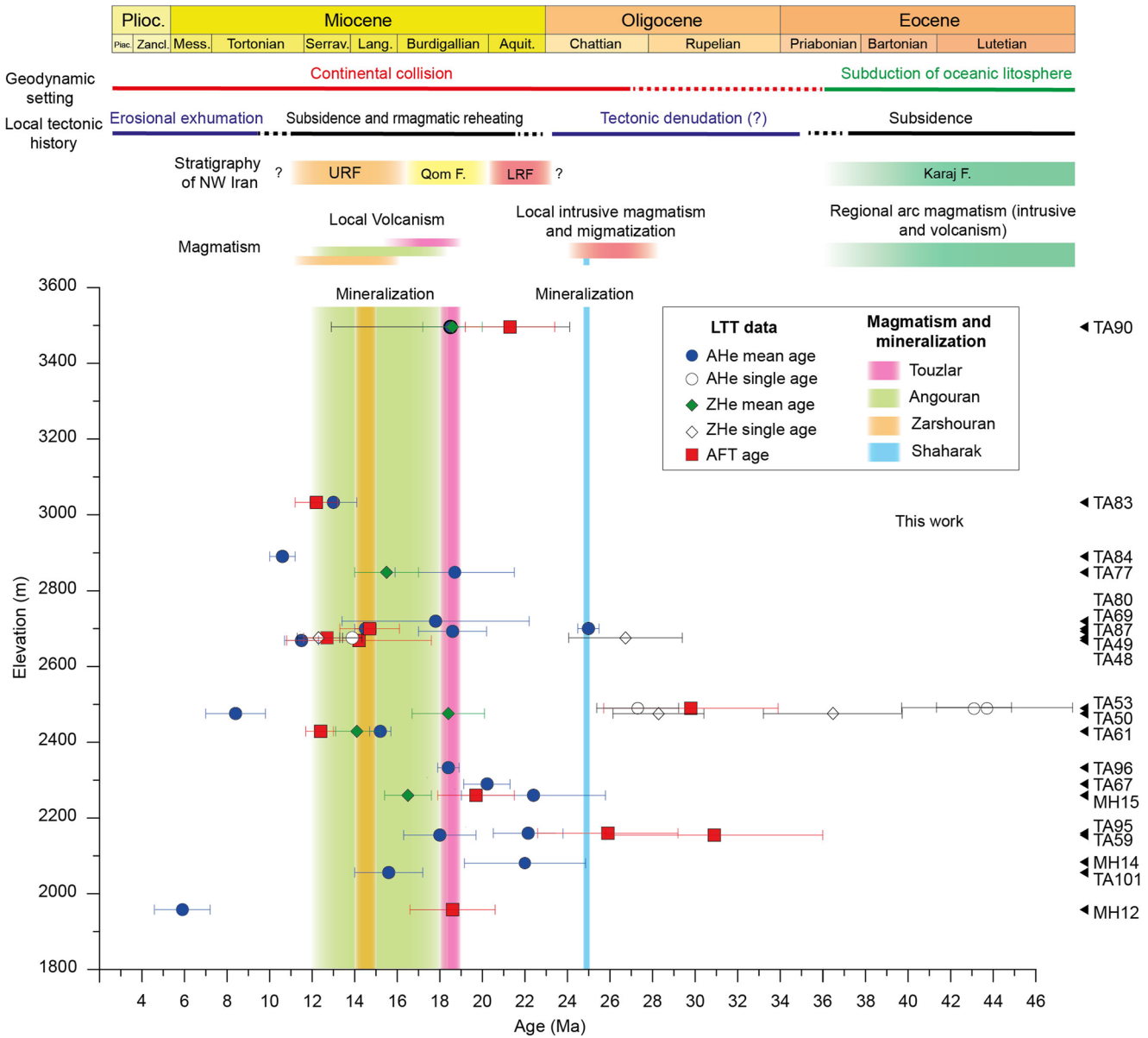
Figure 9. (a) Age-elevation plot of AHe, ZHe, and Apatite Fission Track data. For the age intervals of the mineralization processes see Table 1 and reference therein. The local tectonic history reported on top of the figure summarizes the results of this study.

dispersion of 48% (Galbraith & Laslett, 1993; Table S4 and Figure S5 in Supporting Information S1). Sample TA53 exhibits a grain age distribution with two age peaks at 20.7 ± 3.8 and at 70 ± 31 Ma (Figure S5 in Supporting Information S1). The same sample yielded overdispersed AHe ages ranging from 27.1 to 61.9 Ma. The rest of the AHe samples present mean ages that cluster either around 17–20 or 25–26 Ma.

2. Samples from the eastern TRC margin (7 samples; TA80, TA87, TA96, TA101, MH12, MH14, and MH15) were collected between ∼2.0 and 2.7 km of elevation, and exhibit AHe mean ages ranging from 15.6 to 22.4 Ma and two AFT ages of 19.7 and 18.6 Ma. The exception is represented by a lower Miocene volcanic sample (MH12), which yielded the youngest AHe aliquot ages of the entire data set (mean age of 5.9 Ma).

3. Samples from the axial sectors of the TRC (5 samples; TA61, TA69, TA77, TA83, and TA84, hanging wall of the Chahartagh Fault) display AHe ages varying from 18.7 to 10.6 Ma and ZHe and AFT ages of ∼15 and 14–12 Ma, respectively, over an elevation of ∼2.4–3 km. Sample TA69, which was collected close to the Chahartagh Fault, yielded an AFT central age of 14.7 ± 1.4 Ma with a grain age distribution failing the P(χ)^2 test and with two age peaks at 11.0 ± 0.9 and 22.5 ± 2.4 Ma (Figure S5 in Supporting Information S1).

4. The western TRC margin (3 samples, TA48, TA49 and TA50, footwall of the Chahartagh Fault) presents the youngest AHe ages ranging from 11.5 to 8.4 Ma at a uniform elevation of ~2.6 km and the paired AFT ages range from 14.2 to 12.7 Ma. In this sector, the paired ZHe ages yielded the oldest ages of the entire data set with single aliquot ages ranging from 36.2 to 12. 3 Ma.

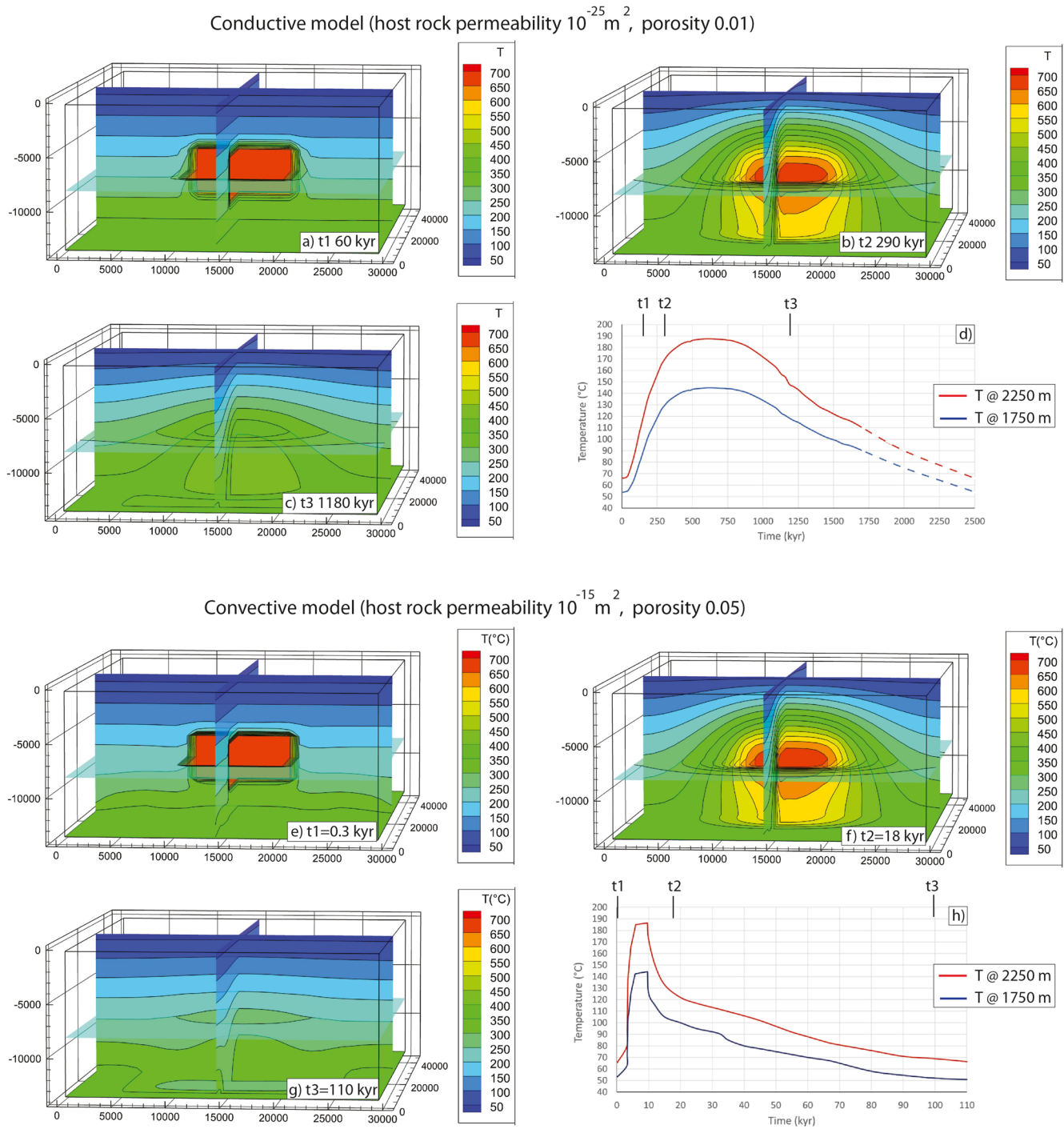## 6. Numerical Thermal Modeling

6.1. Motivations

Our LTT ages from different thermochronometers (with associated errors) overlap within the same sample and among different samples collected at various elevation (Figure 9). Furthermore, the early middle Miocene LTT ages are coeval with regional subsidence associated with the deposition of a sedimentary cover of limited thickness (2 km at maximum, at least along the eastern TRC; Figure 9). This thickness would not be enough to reset most of our thermochronometers. Combined, these data indicate that our LTT data set cannot record cooling associated with erosional exhumational (i.e., removal of rocks through erosion during rock uplift induced by contraction) or tectonic denudation (i.e., removal of rocks along major fault planes during normal faulting and crustal thinning). An alternative mechanism that may explain the observed LTT ages is the intrusion of igneous bodies in the middle-upper crust (e.g., Caggianelli et al., 2013; Murray et al., 2018). This process can lead to a transient perturbation of the isotherms with a pulse of heating followed by cooling. Heat transfer will occur through thermal conduction and convection of fluids circulating in porous and fractured host rocks (e.g., Norton & Taylor, 1979; Parmentier & Schedl, 1981; Turcotte & Schubert, 2002). The occurrence of convection is more evident in metallogenic districts where fluids rising along faults and fracture zones or highly permeable rocks lead to localized mineralization processes (e.g., Fu et al., 2010; Luijendijk, 2019; Sánchez et al., 2021). To explore and quantify the transient thermal effect of magmatic intrusions on host rocks (i.e., the spatial distribution, magnitude, and timing of the perturbation with and without fluids), we designed a forward, 3D numerical thermal model using the TOUGH2 code (Transport Of Unsaturated Groundwater and Heat; W. M. Kissling, 1995; Pruess, 1991, https://tough.lbl.gov/). This code is commonly used for characterizing geothermal reservoirs and can simulate conductive heating/cooling and fluids flow in porous and fractured media. Specifically, first, we simulated a prevailing conductive heating/cooling process imposing low permeability and porosity on the host rocks (here defined as "conductive model"; Figure 10a), and then we run another model imposing a higher value of permeability and porosity to simulate uniform convective heating/cooling process (here defined as "convective model"; Figure 10b).

6.2. Methods

The thermal model was performed on a crustal block with a size of 30 × 45 km and a depth of 14 km. The modeled volume was divided into 37,800 elements (each $1.0 \times 1.0 \times 0.5$ km) to allow relatively fast model runs while preserving a reasonable accuracy. The model was run using a super-critical version of the TOUGH2 code (W. M. Kissling, 1995; Pruess, 1991). At the onset of the model, the pressure gradient was taken as hydrostatic computed with an initial geothermal gradient of 25°C/km (McKenzie & Priestley, 2008). A Dirichlet thermal boundary at constant temperature of ~365°C was used as bottom boundary of the model according to the crustal temperature gradient. The upper boundary of the model was maintained at a constant temperature and pressure (16°C and 25 bars for cells at 250 m depth).

In the "conductive model," to minimize the effect of convection and fluid migration we used relatively low permeability (10^{-25} m^2) and porosity (0.01) values. These values allow a minimal fluid circulation in the host rocks around the pluton avoiding excessive fluid overpressure and hydro-thermal fracturing (e.g., W. Kissling, 1999; Manning & Ingebritsen, 1999). In the "convective model," to account for advection, we used a permeability of 10^{-15} m^2 and a porosity of 0.05. These values are typical of sandstones reservoirs with a rather low permeability (e.g., Lis-Śledziona, 2019) and are slightly higher than the permeability estimates of metamorphic rocks in the upper crust (10^{-16}–10^{-20} m^2) (Manning & Ingebritsen, 1999). Consequently, our two models can be considered as two end-member scenarios of pure conduction and uniform convection.

To illustrate the first-order effects of a magma intrusion on the thermal state of the upper crustal block, a pluton was emplaced in the central model domain at a depth of 6 km. This is consistent with estimates from the emplacement depth of the Oligocene plutons exposed on the surface (Hajialioghli et al., 2011; Saki et al., 2012). The

Figure 10. Thermal modeling results for the (a–c) conductive and (e–g) convective models. Time versus temperature (t-T) plots for two reference points placed above the center of the pluton at 2.25 and 1.75 km of depth for the (d) conductive and (h) convective models. The dashed lines of panel (d) represent the extrapolated time-temperature path for the last part of the conductive model.

pluton is approximated by the geometry of a rectangular prism having a dimension of 10×5 and 5 km of depth, with a bulk composition resembling a quartz monzonite, like the ~25-Myr-old-pluton emplaced along the southern sectors of the TRC (see sample TB18 of Sepahi et al. (2020)). Our modeling approach, however, reduces the complex process of magma emplacement to a simple instantaneous thermal event. The heat capacity of the host rock is increased to account for latent heat effects, and the thermal properties of the rock were assigned based on

the rock composition reported in Sepahi et al. (2020). The first thermal model assumes conductive cooling with a limited effect of fluid circulation and considers the latent heat of magma crystallization. The second model, with 10^{-15} m^2 host rock permeability was carried out to compare the effect of advective cooling that is expected to greatly reduce the pluton cooling time. The model parameters are summarized in Table S5 in Supporting Information S1.

6.3. Results

Our numerical thermal model allows to broadly quantify the thermal effect (transient heating and cooling), of a magmatic intrusion on almost impermeable ("conductive model") and permeable ("convective model"; Figure 10) host rocks. Both models show a significant perturbation of the geothermal field. The main difference between the two models is represented by the rate and the duration of heating/cooling. This can be better appreciated by looking at the temperature-time plots of two reference points at 1.75 and 2.25 km of depth above the plutons (Figures 10d and 10h, respectively). These two points represent depths located slightly above and below the isotherm corresponding to the nominal closure temperature of the AHe system before the thermal perturbation. They are representative of our data set because our samples present ages that are mostly older than the age of the final exhumation (10–11 Ma). Consequently, before 11–10 Ma, most of our samples were at depths shallower than the depth representing the closure temperature of AHe the system. This conclusion is supported by the thickness of the preserved Miocene sediments that is generally lower than 2 km and hence insufficient to reset (through burial) the AHe system.

In the "conductive model," temperatures >140°C and >180°C at 1.75 and 2.25 km of depth, respectively, are reached after ~415.000 years and last for ~485.000 years (Figure 10d). The peak temperatures recorded at the two investigated depths are ~144°C and 188°C. In the "convective model," temperatures >140°C and >180°C, at 1.75 and 2.25 km of depth, respectively, are reached after ~4,700 and ~5,500 years and last for ~5,300 and 5,500 years, respectively (Figure 10h). Although we observe two orders of magnitude of difference in time, the peak temperatures for "convective model" (~144°C and ~186°C at 1.75 and 2.25 km) are very similar to those of the conductive one. These temperatures indicate an increase in the geothermal gradient from 25°C/km to a maximum mean value of ~80°C/km. This range of values is consistent with the geothermal gradients of regions characterized by shallow intrusion such as the Larderello geothermal field in Tuscany, Italy, where temperature >200°C can be found at a depth of 1.5 km (Della Vedova et al., 2008). Similar thermal conditions have been also described in magmatic arcs (e.g., Japan, Tanaka et al., 2004), active and passive continental rifts (e.g., Upper Rhine Graben, Pauwels et al., 1993; Ethiopia, Gianelli & Teklemariam, 1993), orogenic plateaus and collisional orogens (e.g., Tibet, Zhu et al., 2015; Puna-Altiplano, Hamza & Muñoz, 1995; Central Anatolia, Ates et al., 2005).

In both models, the cooling rates are lower than the heating rates (up to 30 times). In the "conductive model," after 1,600 kyr the geothermal field has not returned to the starting conditions (Figure 10a). At that time, the temperatures in the two reference points are still 50%–60% higher than the original temperatures. The initial temperature conditions are most likely reached after ~2,500 kyr from the thermal perturbation. In the "convective model" the initial temperatures are reached after ~95 and ~110 kyr from the thermal perturbation for the shallowest (1.75) and the deepest (2.25 km) reference point, respectively.

6.4. Limitations of the Thermal Modeling

Our thermal models simulate the spatio-temporal perturbation of the isotherms induced by transient heating but do not predict the associated LTT cooling ages. The effect of reheating on a LTT data set will be investigated in Section 7. Furthermore, our model does not include rock uplift and the removal of rocks through erosional or tectonic exhumation. In particular, the occurrence of uplift and exhumation during reheating is expected to increase the rates of cooling as shown by Caggianelli et al. (2013). Nevertheless, our approach is appropriate for the TRC because volcanism and igneous intrusions occurred mostly during moderate subsidence rather than exhumation associated with topographic growth.

Finally, our "convective model" is designed for a setting with uniform permeability and does not consider permeability variations induced by fractures and/or faults. The occurrence of permeability anisotropies would localize the fluids trajectories adding more complexities to the spatio-temporal pattern of heating/cooling. Consequently,

the effect of igneous intrusions on the host rocks will be more difficult to interpret because it will be function of the geometry and density of the fractures (e.g., W. M. Kissling et al., 2015). Additional complications may be associated with mineral precipitation within the fractures, which may alter the rock permeability through time (e.g., Battistelli et al., 1997). Our goals, however, are beyond the understanding of the impact of reheating along and across pre-existing fault zones. Future field-based, thermochronologic, geochronologic, and modeling studies will elucidate the effect of faults and highly fractured rocks on a LLT data set.

7. Interpretation of the LTT Data Set

Our numerical thermal model predicts the spatio-temporal distribution of heat in the shallow crust during the emplacement of igneous bodies. The modeled heat pattern suggests that the transient upward and downward movement of the isotherms has the potential to impact LTT ages. To fully reset any LTT system, however, the temperature must be higher than the closure temperature for a sufficient time. Although the magnitude of heating in the two thermal models is similar, the timing of heating/cooling in the "convection model" is two orders of magnitude faster than in the "conductive model" (Figure 10). Therefore, the two models may have a different influence on the same LTT system. To test if: (a) the modeled thermal perturbations could reset LTT data and (b) reheating could explain our LTT ages, we designed a forward model with HeFty (Ketcham, 2005; see Murray et al., 2022 and references therein for a recent review). The forward model is based on geological constraints and observations reported below.

The TRC has experienced multiple events of uplift and exhumation that led to the exposure of the crystalline basement as documented by the nonconformity stratigraphic contacts with the Eocene and the Oligo-Miocene sediments. Independently from the mechanisms that produced basement exhumation (i.e., tectonic denudation vs. erosional exhumation, see Section 8), our forward thermal histories are based on geological data and observations reported in Sections 2 and 3 and include the following steps (Figure 11): (a) fast cooling started at ~32–30 Ma from temperature greater than 200°C and was associated with several km of exhumation; (b) the crystalline basement exposed on the surface experienced limited subsidence from ~22–20 to (at least) 11–10 Ma; (c) reheating occurred during subsidence and sediment burial (see details concerning two reheating scenarios in Section 7.2); (d) slow erosional cooling from shallow depth took place sometime after 11–10 Ma (see details in Section 8.4).

7.1. Effect of Thermal Perturbations on ZHe, AFT, and AHe Systems

To test the effect of reheating on LTT ages we set up four forward models where we imported in HeFTy the time-temperature (t-T) paths reported in Figures 10d and 10h (see also Figure S6 in Supporting Information S1). For the ZHe and AHe data we used the mean spherical radius (Rs) and mean uranium content (eU) of our analyzed samples that yielded reliable ages (Zircon: Rs = 53 μm, eU = 581 ppm and Apatite: Rs = 53 μm, eU = 89 ppm). For the AFT data we considered the mean Dpar (2.4 μm) of the analyzed samples and the c-axis projected lengths. The forward modeling results reported in Table 3 show that only the t-T path from the "conductive model" at 2.25 km yields an almost fully reset ZHe age (13.8 instead of 12.5 Ma). The rest of the imported t-T paths gave modeled ZHe ages that are unaffected by reheating. Conversely, the AFT ages are fully reset for both t-T paths of the "conductive model" and for the t-T path of the "convective model" at 2.25 km of depth. Finally, the AHe are fully reset for all the t-T paths. Overall, our modeling setup shows that the intrusion of an igneous body can affect the LTT ages of samples located at ~2 km of depth. In particular, the AHe ages will be always reset, while the AFT and ZHe ages will be affected by reheating only under certain circumstances. This because the t-T paths of the conductive and convective models represent two end-member reheating scenarios that are function of rock permeability. As rock permeability diminishes, the heating time increases and a transition from partially to fully reset AFT and ZHe ages will occur.

7.2. Effect of the Reheating Scenarios on Our LTT Data Set

To test if our LTT ages could be explained by reheating we designed a forward modeling strategy with HeFTy based on the regional thermal history reported in Figure 11a. In particular, we imposed two reheating scenarios according to the age of the major mineralization events (Table 1). In scenario 1, reheating is maximum at ~18 Ma, which is approximately the age of the oldest Miocene volcanics (Touzlar mineralization, the eastern TRC; Figures 2 and 9). In scenario 2, reheating peaks at ~13 Ma, which is approximately the age of the youngest
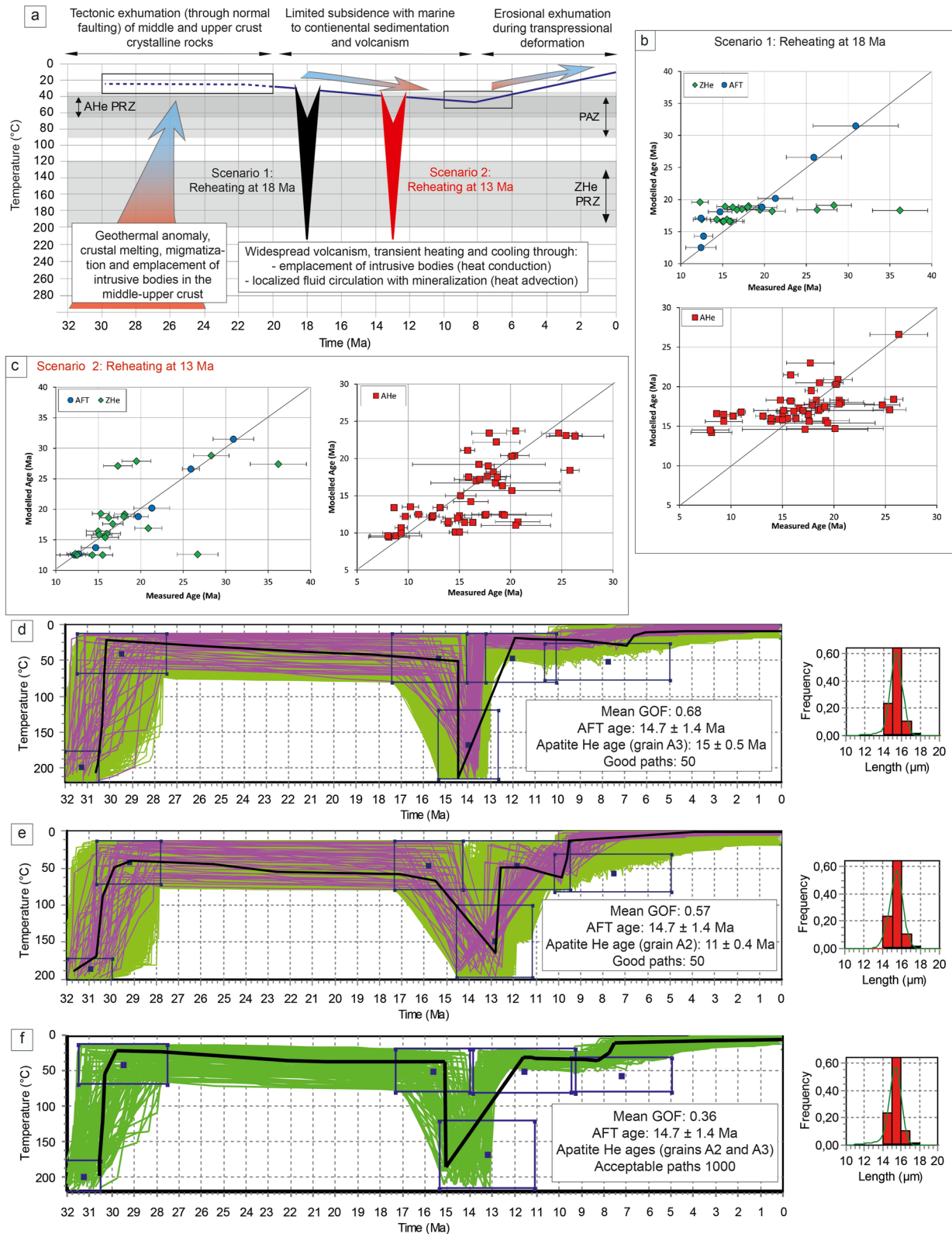
Figure 11. (a) Time-temperature diagram displaying the boundary conditions of the forward thermal modeling (see text for details). Forward modeling results presented as measured versus modeled low-temperature thermochronology ages for reheating at (b) 18 and (c) 13 Ma; AHe and ZHe data are modeled as single grain ages. Inverse modeling results for sample TA69, with acceptable (green) and good (magenta) time-temperature paths and best-fit model (black) using single (A3 and A2; panels (d and e), respectively) and multiple (g) AHe aliquots.

Table 3
HeFTy Forward Modeling Results for Reheating at 13 Ma

	Conductive at 2.25 km (max T pre-perturbation: 66°C; peak T 188°C)	Conductive at 1.75 km (max T pre-perturbation: 54°C; peak T 145°C)	Convective at 2.25 km (max T pre-perturbation: 66°C; peak T 187°C)	Convective at 1.75 km (max T pre-perturbation: 53°C; peak T 144°C)
ZHe (Ma)	14.2	29	29.4	30.8
AFT (Ma)	12.1	12.7	12.7	26.7
MTL (μm)	15.01 ± 0.89	15.11 ± 0.86	15.02 ± 0.79	14.07 ± 1.29
AHe (Ma)	9.4	10.7	9.5	11.6

Note. For the thermal perturbation we imported the temperature time paths from the conductive and the convective numerical thermal models of Figure 10 at 2.25 and 1.75 km of depth (Figure S6 in Supporting Information S1). Details of the thermal history before and after the reheating event are summarized in Figure 11 and are reported in Section 7.

Miocene volcanics (Angouran and Zarshouran mineralization; central-western TRC; Figures 2 and 9). The two modeled reheating events, however, can be considered two end-member scenarios, given the age of the local Miocene magmatism (Table 1 and Figure 9). Moreover, more than one thermal perturbation may have occurred within the entire TRC. Consequently, some of our ages could reflect the effect of multiple thermal events. Each modeled scenario lasted <∼2.5 Myr (Table 3). The input data for each forward model include ZHe and AHe single grain ages and AFT data (central ages; track length only for sample TA69; Table S6 in Supporting Information S1). For both scenarios, we explored a range of peak temperatures varying between 70°C and 250°C with steps of 10°C. In Table S6 in Supporting Information S1, Figures 11b and 11c we report, for each sample, the results of the forward model that generated the highest combination of GOF values among the used LTT systems for all analyzed grains. Sample TA53 was not modeled because it presents overdispersed single grain AHe ages. Samples TA48 and MH105 where not modeled because they are not crystalline basement rocks (Table 2).

Although in several samples the forward model does not predict all single grain ZHe and AHe ages, in most of the samples we observe a relatively good match between measured and predicted ages (Figures 11b and 11c). This match is more evident for the 13-Myr-old reheating scenario where 59% and 38% of the modeled ages have GOF >0.1 and 0.5, respectively (Table S6 and Figure S7 in Supporting Information S1). For the 18 Ma reheating scenario, 58% and 32% of the modeled ages have GOF >0.1 and 0.5, respectively (Table S6 and Figure S8 in Supporting Information S1). The 18 Ma reheating scenario predicts a ZHe and AHe age cluster at 20–15 Ma, but it does not provide a good fit for older and younger cooling ages (Figure 11b and Table S6 in Supporting Information S1). Good fit samples for the 18 Ma scenario are from the eastern (MH14, MH15) and the northern TRC (TA90, TA95; Table S6 in Supporting Information S1; Figure 8). Instead, the 13 Ma scenario exhibits a slightly better fit for different LTT age intervals (Figure 11c; Table S6 in Supporting Information S1). Good fit samples for the 13 Ma scenario are mostly from the western (TA49, TA50), southern (TA59, TA61, TA77), and central TRC (TA69, TA83, TA84; Table S6 in Supporting Information S1; Figure 8). Samples with only AHe data can be modeled with both reheating scenarios (see similar GOF of samples TA67, TA80, TA87, TA96, TA101; Table S6 in Supporting Information S1).

To further corroborate the reheating hypothesis for our LTT ages, we performed HeFTy inverse modeling of the best constrained sample (TA69). This sample is the only one with track length and AFT age data and includes also three AHe single ages that do not reproduce well (STDEV 3.3 Myr over a mean age of 14.5 Ma). Instead of using the AHe mean age, we model the two youngest single ages separately (Figures 11d and 11e) and together (Figure 11f) imposing the 13 Ma reheating scenario. Models with single AHe ages present good t-T paths (GOF > 0.5, Figures 11d and 11e), while the model with both AHe ages yields only acceptable paths (GOF > 0.1, Figure 11f). These results are consistent with the reheating hypothesis.

Overall, we conclude that our LTT data set can be interpreted as a record of thermal perturbations induced by igneous intrusions, at peak temperatures and for a duration that is consistent with the output of our TOUGH2 model. Reheating occurred between ∼18 and ∼13 Ma, most likely before the onset of exhumation that should have started after 11–10 Ma. Finally, the reheating scenario can also explain why some of our samples have AHe ages that are slightly older than the paired AFT ages (e.g., TA61 and MH15; Table 2 and Figures 8 and 9). Specifically, Reiners (2009) demonstrated that during thermal pulses (<10^6 years) such as short-lived magmatic

or fluid-advections events, the occurrence of non-monotonic cooling may resulti in a complete AFT resetting and only a partial AHe resetting (i.e., kinetic cross-over; Reiners, 2009). Consequently, the AFT ages, which in our forward model present a rather good fit for both reheating scenarios (Figures 11b and 11c) may be better recorder of the timing of reheating events than the paired AHe ages.

8. Evolution of the TRC Metallogenic District

8.1. Late Cretaceous to Paleocene Erosional Exhumation

The oldest Cenozoic deposits covering the upper Neoproterozoic metamorphic basement are Eocene clastics exposed along the southern TRC margin, that are coeval with the volcanics of the Eocene magmatic flare up (Figures 2 and 3, Verdel et al., 2011). This configuration suggests that the removal of the Paleo-Mesozoic sedimentary cover and part of the basement (at least in the southern TRC) must have occurred before the Eocene, rather than during tectonic denudation associated with the Eocene magmatic flare up as observed in other sectors of the upper plate (Karagaranbafghi et al., 2012; Verdel et al., 2007). The timing and mechanisms of this episode of exhumation, however, are poorly constrained, because our samples have been thermally overprinted during the Oligo-Miocene and because older tectonic structures have been obliterated by collisional deformation. Late Cretaceous to Paleocene exhumation has been also observed in northern (Talesh, Alborz and Kopeh Dagh mountains; e.g., Ballato et al., 2011; Guest et al., 2006; Madanipour et al., 2017; Robert et al., 2014), and central Iran (e.g., Berberian & King, 1981; Stöcklin, 1968; Tadayon et al., 2018), where it has been linked to a regional phase of compressional deformation. Moreover, this event of deformation is coeval with the development of a foreland basin over the northern margin of the Arabian Plate associated with ophiolite obduction (Homke et al., 2009). Overall, these observations suggest that exhumation was probably related to variations in the geodynamic boundary conditions along the entire Neo-Tethys subduction zone (Agard et al., 2014; Boutoux et al., 2021). Thus, we favor erosional exhumation induced by contractional tectonics as the major cause for the latest Mesozoic earliest Cenozoic unroofing observed in the southern TRC.

8.2. Oligocene to Possibly Early Miocene Thermal Anomaly and Tectonic Denudation (∼29 to 22–20 Ma)

The Oligocene represents a rather enigmatic period in the geological history of the Eurasian upper plate of Iran because the stratigraphic record, which is represented by the LRF, is discontinuous and poorly dated (e.g., Berberian & King, 1981). Available petrological data indicate that during the Oligocene, the metamorphic basement of the TRC was characterized by: (a) formation of localized migmatitic gneisses, (b) emplacement of small size granitoids and fractures/dikes filled by leucosome formed during the partial melting of the crystalline basement, and (c) emplacement of large plutons like the Almalou and Shahrak intrusives, which were previously mapped as Neoproterozoic basement or Triassic/Jurassic granitoids (Babakhani & Ghalamghash, 1998; Hajialioghli et al., 2011; Moazzen et al., 2013; Saki et al., 2012; Shafaii Moghadam et al., 2016, 2017; Figures 2 and 8). The metamorphic conditions that led to migmatization and the development of a leucosome through the melting of metamorphosed middle crust rocks (mostly amphibolites) are estimated to be 750°C–800°C and 5–7.5 kbar, corresponding to 13.5–20 km of depth assuming a density of overlaying rocks of 2.7 g/cm^3 (Shafaii Moghadam et al., 2016). This crustal melt was injected at depths of 9.5–13.5 km (subsolidus magmatic conditions of 650°C–600°C and 5–3.5 kbar; Hajialioghli et al., 2011). Locally, these intrusive bodies produced contact metamorphism that overprinted the regional Pan-African metamorphism at peak conditions of ∼580°C and ∼3–4 kbar, suggesting a depth of 8–11 km and a geothermal gradient of 50°C/km–70°C/km (Saki et al., 2012). This Oligocene to possibly early Miocene thermal activity has been also recorded in the host rock of the Zarshuran and Angouran mines (Figure 2), where a few mica and whole rock Ar-Ar ages record a phase of resetting between 27 and 20 Ma (Table 1 and Figure 8). Overall, these data indicate that between 29 and 22–20 Ma the TRC experienced a large thermal anomaly that led to widespread partial melting of the middle crust with the formation of magmatic bodies emplaced around 8–13 km of depth.

These middle to upper crustal rocks are overlain by red clastics of the LRF and lower Miocene volcanic, volcaniclastic and marine deposits of the Qom Formation (Figures 2 and 4). This implies a removal of an up to 8- to 13-km-thick section of crystalline rocks, and possibly a part of its Phanerozoic cover, between 29 and 22–20 Ma at rates >1 mm/yr. These values appear to be rather elevated for erosional exhumation during contractional deformation (especially if we consider the lack of coeval clastic deposits), although a phase of Oligocene regional

compression in response to the earliest stages of the Arabia-Eurasia collision has been observed in the lower (e.g., Homke et al., 2009; Pirouz et al., 2017) and upper plate (e.g., Ballato et al., 2011; Madanipour et al., 2017; Robert et al., 2014). Thus, basement exhumation could have been driven by tectonic denudation (Hassanzadeh et al., 2008; Moazzen et al., 2013; Shafaii Moghadam et al., 2016, 2017; Stockli et al., 2004) as observed in several metamorphic domes where low-angle normal faults are closely associated with in situ crustal melting (e.g., Schmidt et al., 2011; Stübner et al., 2013). These older extensional structures, however, are difficult to detect in the field because they juxtapose different sectors of the crystalline basement and/or because they have been obliterated by younger contractional deformation.

In conclusion, we interpret the Oligocene cooling ages as a record of tectonic denudation (i.e., controlled by normal faulting). It should be noted, however, that the southern and south-western sectors of the TRC were already exhumed, because the Eocene sedimentary cover overlays the crystalline basement (Figure 3). This agrees with the occurrence of a few early Cenozoic partially reset to unreset AHe and AFT ages (TA53, TA59, and TA57) indicating that the Oligocene exhumation of deep crustal rocks through normal faulting must have been very localized rather than a regional feature (see discussion in Paknia, Ballato, Heidarzadeh, Cifelli, Oskooi, et al. (2021)).

8.3. Miocene Reheating During Magmatism and Sedimentary Burial (~22–20 to 11–10 Ma)

As discussed in Section 7, our LTT ages could be explained through transient heating induced by shallow intrusions sometime between 18 and 13 Ma during regional subsidence. Although plutons of Miocene age have not yet been exhumed (except for the middle-late Miocene shallow intrusions exhumed along the SE sectors of the TRC; Figure 2) their potential emplacement is suggested by the occurrence of widespread volcanism and mineralization (Table 1). The thermal perturbations should have been induced by heat conduction and convection (Figure 10), where the latter could have been facilitated by the syn-sedimentary normal faults (Figure 7). Our field data, however, are too sparse to elucidate any spatio-temporal pattern of extension and the importance of normal faults in controlling volcanic activity during contractional, collisional deformation.

8.4. Late Miocene to Present Erosional Exhumation and Evolution of the Chahartagh Fault (After ~11–10 Ma)

Stratigraphic data indicate that the most recent event of basement exhumation should have started sometime after the deposition of the middle-upper Miocene URF (Figure 2). In the Great Pari Basin, to east of the TRC (Figure 2), the URF strata are superseded by a ~10.7-Myr-old sheet of conglomerates marking the start of exhumation in the nearby sediment source area (Tavaq conglomerates, Ballato et al., 2017). Conglomerate clasts include metamorphic rocks like those exposed in the TRC (Ballato et al., 2017). Similarly, in the central sectors of the TRC (Angouran mine area) the youngest volcanics that experienced contractional deformation are 10 ± 1 Ma (Daliran et al., 2013; Table 1). This is also consistent with the occurrence of ~11 Myr old intrusive rocks interbedded within the URF in the south-western sectors of the TRC (Heidari, 2013; Mehrabi et al., 1999). Collectively, these stratigraphic constraints suggest that basin uplift and erosion started after 11–10 Ma, and hence our late Miocene to early Pliocene LTT ages must have recorded erosional cooling during rock uplift induced by collisional deformation (see samples TA49 and TA50). Considering that the late Miocene cooling ages represent the most recent, but also the least abundant ages (Figure 9), the magnitude of associated exhumation must have been 2 km at maximum in most of the TRC.

Concerning the mechanisms that led to the recent topographic growth and the erosional exhumation of the TRC, we should refer to the structural characteristics described in Section 3. The range is characterized by a set of NW-SE striking, SW-verging sigmoidal reverse faults, and an en-echelon array of folds to the east and the west of Chahartagh Fault, respectively. Importantly, the sigmoidal thrusts join the Chahartagh Fault suggesting a possible genetic link. Furthermore, the TRC is oblique to the Neogene regional contractional direction (McQuarrie & van Hinsbergen, 2013), suggesting that this zone must have accommodated oblique shortening across a wide zone. Wide oblique shear zones generally evolve through progressive fault localization associated with strain weakening until a master fault develops (e.g., Tikoff & Teyssier, 1994). Typical examples of these processes include the North Anatolian Fault (Sengor et al., 2005), the Dead Sea Fault (Nuriel et al., 2017), and the Kuh-e-Faghan Fault in central-eastern Iran (Calzolari et al., 2015) among others. Specifically, for the North Anatolian Fault oblique
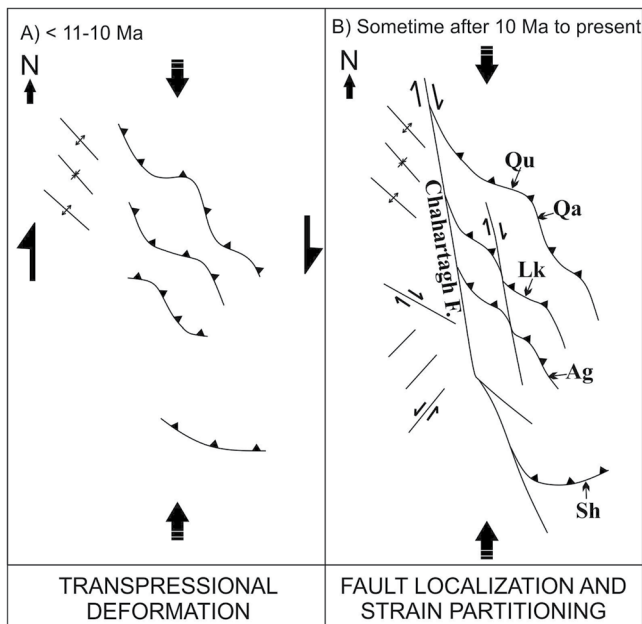
Figure 12. Evolutionary sketch in map view for the Takab Range Complex showing (a) right-lateral transpressional deformation along the Chahartagh Shear Zone, followed by (b) strike-slip faulting along the master Chahartagh Fault. Black arrows show direction of compression and lateral shear. For the (approximate) horizontal scale see Figure 2.

shearing started 12–11 Myr ago in eastern Anatolian along a wide shear zone of transpressional deformation while a well-established through-going strike-slip fault formed only during the last 4 Ma (e.g., Sengor et al., 2005). In the case of the Chahartagh Fault, the accommodation of oblique shortening across a wider shear zone should have started sometime after 11–10 Ma and hence the master, right-lateral, strike-slip Chahartagh Fault could be more recent (Figure 12).

9. Conclusions

This study highlights the impact of magmatic activity on a LTT data set consisting of ZHe, AHe, and AFT data. Our thermal numerical models performed with the TOUGH2 code indicate that the occurrence of magmatic intrusions emplaced in the middle-upper crust (top pluton at 7 km) can perturb the geothermal gradient of the host rocks for a duration ranging from <2.5 Myr for a "conductive model" to <0.1 Myr for a "convective model." These thermal perturbations produce a transient heating up to ~144°C and ~186°C for depths of 1.75 and 2.25 km, respectively. The duration and the magnitude of the reheating can partially or totally reset the investigated LTT systems in rocks at shallow depths (~2 km) that are in an undisturbed situation (e.g., with a steady geothermal gradient of 25°C). These results strongly suggest that a correct interpretation of a LTT data set in an area characterized by protracted and intense magmatic activity requires the combination of multiple thermochronometers, field observations, and geochronologic data. This multidisciplinary approach has allowed interpreting the Cenozoic geologic history of the basement-cored TRC (NW Iran), one of the most productive metallogenic districts of the Arabia-Eurasia collision zone. Although some time windows require additional work, our study documents:

1. Late Cretaceous-early Paleocene erosional exhumation probably associated with compressional deformation as recorded along the entire southern and northern margin of the Neo-Tethys subduction system. This event was followed by the deposition of Eocene clastic deposits onto the exhumed TRC basement (Eocene depositional cycle).
2. Rapid Oligocene to possibly early Miocene (29 to 22–20 Ma) exhumation with the removal of an 8- to 13-km-thick crustal section and the exposure of basement rocks on the surface. This was most likely driven by normal faulting (i.e., tectonic denudation) in association with a thermal anomaly that caused partial melting and migmatization.
3. Limited subsidence from 22–20 (and possibly earlier) to 11–10 Ma with the deposition of continental deposits of the LRF, marine strata and interlayered volcanics of the Qom Formation and red beds of the Upper Red Formation (the Oligo-Miocene depositional cycle). Sediment burial was associated with reheating, sometime between ~18 and ~13 Ma, triggered by the emplacement of shallow intrusions in association with volcanism, mineralization, and minor normal faults.
4. Basin uplift after 11–10 Ma with the erosional removal of a 2- to 3-km-thick section composed of basement rocks and overlaying sediments and volcanics of the Oligo-Miocene depositional cycle. This was associated with the development of a wide transpressional shear zone, that included sigmoidal reverse faults and an en-echelon array of folds, evolving into a master, localized, right-lateral strike-slip fault.

Conflict of Interest

The authors declare no conflicts of interest relevant to this study.

Data Availability Statement

The Supporting Information S1 associated with this article can be accessed at https://doi.org/10.6084/m9.figshare.21425046 and include seven tables (Tables S1–S7 in Supporting Information S1) and eight figures (Figures S1–S8 in Supporting Information S1).

References

Agard, P., Zuo, X., Funiciello, F., Bellahsen, N., Faccenna, C., & Savva, D. (2014). Obduction: Why, how and where, Clues from analog models. *Earth and Planetary Science Letters*, *393*, 132–145. https://doi.org/10.1016/j.epsl.2014.02.021

Allen, M. B., & Armstrong, H. A. (2008). Arabia–Eurasia col-lision and the forcing of mid-Cenozoic global cooling. *Palaeogeography, Palaeoclimatology, Palaeoecology*, *265*(1–2), 52–58. https://doi.org/10.1016/j.palaeo.2008.04.021

Allen, M. B., Kheirkhah, M., Emami, M. H.S., & Jones, J. (2011). Right-lateral shear across Iran and kinematic change in the Arabia-Eurasia collision zone. *Geophysical Journal International*, *184*(2), 555–574. https://doi.org/10.1111/j.1365-246X.2010.04874.x

Ates, A., Bilim, F., & Buyuksarac, A. (2005). Curie point depth investigation of Central Anatolia, Turkey. *Pure and Applied Geophysics*, *162*(2), 357–371. https://doi.org/10.1007/s00024-004-2605-3

Azizi, H., Daneshvar, N., Mohammadi, A., Asahara, Y., Whattam, S. A., Tsuboi, M., & Minami, M. (2021). Early Miocene post-collision andesite in the Takab area, northwest Iran. *Journal of Petrology*, *62*(7), egab022. https://doi.org/10.1093/petrology/egab022

Babakhani, A. R., & Ghalamghash, J. (1998). *Geological map of Takht-e-Soleyman, scale: 1:100,000*. Geological Survey of Iran.

Ballato, P., Cifelli, F., Heidarzadeh, G., Ghassemi, M. R., Dupont-Nivet, G., Balling, P., et al. (2017). Tectono-sedimentary evolution of the northern Iranian Plateau: Insights from middle–late Miocene foreland-basin deposits. *Basin Research*, *29*(4), 1–30. https://doi.org/10.1111/bre.12180

Ballato, P., Uba, C. E., Landgraf, A., Strecker, M. R., Sudo, M., Stockli, D. F., et al. (2011). Arabia–Eurasia continental collision: Insights from late tertiary foreland-basin evolution in the Alborz mountains, northern Iran. *The Geological Society of America Bulletin*, *123*(1–2), 106–131. https://doi.org/10.1130/B30091.1

Barbarand, J., Carter, A., Wood, I. G., & Hurford, A. J. (2003). Compositional and structural control of apatite fission-track annealing. *Chemical Geology*, *198*(1–2), 107–137. https://doi.org/10.1016/S0009-2541(02)00424-2

Battistelli, A., Calore, C., & Pruess, K. (1997). The simulator TOUGH2/EWASG for modeling geothermal reservoirs with brines and non-condensible gas. *Geothermics*, *26*(4), 437–464. https://doi.org/10.1016/S0375-6505(97)00007-2

Berberian, M., & King, G. C. P. (1981). Towards a paleogeography and tectonic evolution of Iran. *Canadian Journal of Earth Sciences*, *18*(11), 210–265. https://doi.org/10.1139/e81-163

Boutoux, A., Briaud, A., Faccenna, C., Ballato, P., Rossetti, F., & Blanc, E. (2021). Slab folding and surface deformation of the Iran mobile belt. *Tectonics*, *40*(6), e2020TC006300. https://doi.org/10.1029/2020TC006300

Braun, J., van der Beek, P., Valla, P., Robert, X., Herman, F., Glotzbach, C., et al. (2012). Quantifying rates of landscape evolution and tectonic processes by thermochronology and numerical modeling of crustal heat transport using PECUBE. *Tectonophysics*, *524*, 1–28. https://doi.org/10.1016/j.tecto.2011.12.035

Caggianelli, A., Ranalli, G., Lavecchia, A., Liotta, D., & Dini, A. (2013). Post-emplacement thermo-rheological history of a granite intrusion and surrounding rocks: The Monte Capanne pluton, Elba Island. Italy. *Geological Society, London, Special Publications*, *394*(1), 129–143. https://doi.org/10.1144/SP394.1

Cai, F. L., Ding, H., Wang, A. K., Laskowski, L., Zhang, B., Zhang, B., et al. (2021). Configuration and timing of collision between Arabia and Eurasia in the Zagros collision zone, Fars, southern Iran. *Tectonics*, *40*(8), e2021TC006762. https://doi.org/10.1029/2021TC006762

Calzolari, G., Rossetti, F., Seta, M. D., Nozaem, R., Olivetti, V., Balestrieri, M. L., et al. (2015). Spatio-temporal evolution of intraplate strike-slip faulting: The Neogene–Quaternary Kuh-e-Faghan Fault, central Iran. *The Geological Society of America Bulletin*, *128*(3–4), 374–396. https://doi.org/10.1130/B31266.1

Daeijavad, H. A., Asadi, H. H., & Mokhtari, A. R. (2020). Identification and application of a Carlin-type gold mineral system for exploration targeting in the Takab geothermal basin, NW Iran. *Ore Geology Reviews*, *121*, 103494. https://doi.org/10.1016/j.oregeorev.2020.103494

Daliran, F., Pride, K., Walther, W., Berner, Z. A., & Bakker, R. J. (2013). The Angouran Zn (Pb) deposit, NW Iran: Evidence for a two stage, hypogene zinc sulfide–zinc carbonate mineralization. *Ore Geology Reviews*, *53*, 373–402. https://doi.org/10.1016/j.oregeorev.2013.02.002

Daneshian, J., & Ramezani Dana, L. (2007). Early Miocene benthic foraminifera and biostratigraphy of the Qom Formation, Deh Namak, Central Iran. *Journal of Asian Earth Sciences*, *29*(5–6), 844–858. https://doi.org/10.1016/j.jseaes.2006.06.003

Darin, M. H., & Umhoefer, P. J. (2022). Diachronous initiation of Arabia–Eurasia collision from eastern Anatolia to the southeastern Zagros Mountains since middle Eocene time. *International Geology Review*, *64*(18), 2653–2681. https://doi.org/10.1080/00206814.2022.2048272

Della Vedova, B., Vecellio, C., Bellani, S., & Tinivella, U. (2008). Thermal modelling of the Larderello geothermal field (Tuscany, Italy). *International Journal of Earth Sciences*, *97*(2), 317–332. https://doi.org/10.1007/s00531-007-0249-0

Dobson, K. J., Stuart, F. M., & Dempster, T. J. (2008). U and Th zonation in Fish Canyon Tuff zircons: Implications for a zircon (U–Th)/He standard. *Geochimica et Cosmochimica Acta*, *72*(19), 4745–4755. https://doi.org/10.1016/j.gca.2008.07.015

Farley, K. (2000). Helium diffusion from apatite; general behavior as illustrated by Durango fluorapatite. *Journal of Geophysical Research*, *105*(B2), 2903–2914. https://doi.org/10.1029/1999JB900348

Flowers, R. M., Ketcham, R. A., Shuster, D. L., & Farley, K. A. (2009). Apatite (U–Th)/He thermochronometry using a radiation damage accumulation and annealing model. *Geochimica and Cosmochimica Acta*, *73*(8), 2347–2365. https://doi.org/10.1016/j.gca.2009.01.015

Fonoudi, M., & Hariri, A. (2000). *Geological map of Takab, scale: 1:100,000*. Geological Survey of Iran.

François, T., Agard, P., Bernet, M., Meyer, B., Chung, S. L., Zarrinkoub, M. H., et al. (2014). Cenozoic exhumation of the internal Zagros: First constraints from low-temperature thermochronology and implications for the build-up of the Iranian plateau. *Lithos*, *206–207*, 100–112. https://doi.org/10.1016/j.lithos.2014.07.021

Fu, F. Q., McInnes, B. I. A., Evans, N. J., & Davies, P. J. (2010). Numerical modeling of magmatic– hydrothermal systems constrained by U–Th–Pb–He time–temperature histories. *Journal of Geochemical Exploration*, *106*(1–3), 90–109. https://doi.org/10.1016/j.gexplo.2009.09.001

Galbraith, R. F., & Laslett, G. M. (1993). Statistical models for mixed fission track ages. *Nuclear Tracks and Radiation Measurements*, *21*(4), 459–470. https://doi.org/10.1016/1359-0189(93)90185-C

Gallagher, K. (2012). Transdimensional inverse thermal history modeling for quantitative thermochronology. *Journal of Geophysical Research: Solid Earth*, *117*(B2), B02408. https://doi.org/10.1029/2011JB008825

Gallagher, K., & Parra, M. (2020). A new approach to thermal history modelling with detrital low temperature thermochronological data. *Earth and Planetary Science Letters*, *529*(1), 115872. https://doi.org/10.1016/j.epsl.2019.115872

Gholami Zadeh, P., Adabi, M. H., Hisada, K.-I., Hosseini-Barzi, M., Sadeghi, A., & Ghassemi, M. R. (2017). Revised version of the cenozoic collision along the Zagros Orogen, insights from Cr-spinel and sandstone modal analyses. *Scientific Reports*, *7*(1), 10828. https://doi.org/10.1038/s41598-017-11042-1

Gianelli, G., & Teklemariam, M. (1993). Water-rock interaction processes in the Aluto-Langano geothermal field (Ethiopia). *Journal of Volcanology and Geothermal Research*, *56*(4), 429–445. https://doi.org/10.1016/0377-0273(93)90007-E

Gilg, H. A., Boni, M., Balassone, G., Allen, C. R., Banks, D., & Moore, F. (2006). Marble-hosted sulphide ores in the angouran Zn–(Pb–Ag) deposit, NW Iran: Interaction of sedimentary brines with a metamorphic core complex. *Mineralium Deposita*, *41*, 1–16. https://doi.org/10.1007/s00126-005-0035-5

Gleadow, A. J. W. (1981). Fission-track dating methods: What are the real alternatives? *Nuclear Tracks*, *5*(1–2), 3–14. https://doi.org/10.1016/0191-278X(81)90021-4

Green, P. F., & Duddy, I. R. (1989). Some comments on paleotemperature estimation from apatite fission tracks analysis. *Journal of Petroleum Geology*, *12*(1), 111–114. https://doi.org/10.2138/rmg.2005.58.3

Guenthner, W. R., Reiners, P. W., Ketcham, R. A., Nasdala, L., & Giester, G. (2013). Helium diffusion in natural zircon: Radiation damage, anisotropy, and the interpretation of zircon (U-Th)/He thermochronology. *American Journal of Science*, *313*(3), 145–198. https://doi.org/10.2475/03.2013.01

Guest, B., Axen, G. J., Lam, P. S., & Hassanzadeh, J. (2006). Late Cenozoic shortening in the west-central Alborz Mountains, northern Iran, by combined conjugate strike-slip and thin-skinned deformation. *Geosphere*, *2*(1), 35–52. https://doi.org/10.1130/GES00019.1

Gülyüz, E., Durak, H., Özkaptan, M., & Krijgsman, W. (2020). Paleomagnetic constraints on the early Miocene closure of the southern Neo-Tethys (Van region; East Anatolia): Inferences for the timing of Eurasia-Arabia collision. *Global and Planetary Change*, *185*, 103089. https://doi.org/10.1016/j.gloplacha.2019.103089

Hajialioghli, R., Moazzen, M., Droop, G., Oberhänsli, R., Bousquet, R., Jahangirii, A., & Ziemann, M. (2007). *Serpentine polymorphs and PT evolution of metaperidotites and serpentinites in the Takab area* (Vol. 71, pp. 203–222). Mineralogical Magazine - MINER MAG. https://doi.org/10.1180/minmag.2007.071.2.203

Hajialioghli, R., Moazzen, M., Jahangiri, A., Oberhansli, R., Mocek, B., & Altenberger, U. (2011). Petrogenesis and tectonic evolution of metaluminous sub-alkaline granitoids from the Takab Complex, NW Iran. *Geological Magazine*, *148*(2), 250–268. https://doi.org/10.1017/S0016756810000683

Hamza, V. M., & Muñoz, M. (1995). Heat flow map of South America. *Geothermics*, *25*(6), 623–646. https://doi.org/10.1016/S0375-6505(96)00025-9

Harangi, S., Lukacs, R., Schmitt, A. K., Dunkl, I., Molnar, K., Kiss, B., et al. (2015). Constraints on the timing of Quaternary volcanism and duration of magma residence at Ciomadul volcano, east-central Europe, from combined U-Th/He and U-Th zircon geochronology. *Journal of Volcanology and Geothermal Research*, *301*, 66–80. https://doi.org/10.1016/j.jvolgeores.2015.05.002

Hassanzadeh, J., Stockli, D. F., Horton, B. K., Axen, G. J., Stockli, L. D., Grove, M., et al. (2008). U–Pb zircon geochronology of late Neoproterozoic–Early Cambrian granitoids in Iran: Implications for paleogeography, magmatism, and exhumation history of Iranian basement. *Tectonophysics*, *451*(1), 71–96. https://doi.org/10.1016/j.tecto.2007.11.062

Hatzfeld, D., & Molnar, P. (2010). Comparisons of the kinematics and deep structures of the Zagros and Himalaya and of the Iranian and Tibetan Plateaus and geodynamic implications. *Reviews of Geophysics*, *48*(2), RG2005. https://doi.org/10.1029/2009RG000304

Heidari, S. M. (2013). *Geology, geochronology and source of Touzlar, Arabshah and Ghozalbolagh gold occurrences in Qorveh-Takab region*, Phd thesis (p. 450). Tarbiat Modares University.

Heidari, S. M., Daliran, F., Paquette, J. L., & Gasquet, D. (2015). Geology, timing, and Genesis of the high sulfidation Au (–Cu) deposit of Touzlar, NW Iran. *Ore Geology Reviews*, *65*(2), 460–486. https://doi.org/10.1016/j.oregeorev.2014.05.013

Homke, S., Verges, J., Serra-Kiel, J., Bernaola, G., Sharp, I., Garcés, M., et al. (2009). Late cretaceous Paleocene formation of the proto-Zagros foreland basin, Lurestan Province, SW Iran. *The Geological Society of America Bulletin*, *121*(7–8), 963–978. https://doi.org/10.1130/B26035.1

Honarmand, M., Xiao, W., Nabatian, G., Blades, M. L., dos Santos, M. C., Collins, A. S., & Ao, S. (2018). Zircon U-Pb-Hf isotopes, bulk-rock geochemistry and Sr-Nd-Pb isotopes from late Neoproterozoic basement in the Mahneshan area, NW Iran: Implications for Ediacaran active continental margin along the northern Gondwana and constraints on the late Oligocene crustal anatexis. *Gondwana Research*, *57*, 48–76. https://doi.org/10.1016/j.gr.2017.12.009

Hurford, A. J. (1990). Standardization of fission track dating calibration: Recommendation by the fission track working group of the I.U.G.S. Sub commission on geochronology. *Chemical Geology*, *80*(2), 171–178. https://doi.org/10.1016/0168-9622(90)90025-8

Hurford, A. J., & Green, P. F. (1983). The zeta age calibration of fission-track dating. *Chemical Geology*, *41*, 285–317. https://doi.org/10.1016/S0009-2541(83)80026-6

Kaislaniemi, L., Van Hunen, J., Allen, M. B., & Neill, I. (2014). Sub-lithospheric small-scale convection—A mechanism for collision zone magmatism. *Geology*, *42*(4), 291–294. https://doi.org/10.1130/G35193.1

Karagaranbafghi, F., Foeken, J. P. T., Guest, B., & Stuart, F. M. (2012). Cooling history of the Chapedony metamorphic core complex, Central Iran: Implications for the Eurasia–Arabia collision. *Tectonophysics*, *524–525*, 100–107. https://doi.org/10.1016/j.tecto.2011.12.022

Ketcham, R. A. (2005). Forward and inverse modeling of low-temperature thermochronometry data. *Reviews in Mineralogy and Geochemistry*, *58*(1), 275–314. https://doi.org/10.2138/rmg.2005.58.11

Ketcham, R. A., Gautheron, C., & Tassan-Got, L. (2011). Accounting for long alpha-particle stopping distances in (U-Th-Sm)/He geo[1]chronology: Refinement of the baseline case. *Geochimica et Cosmochimica Acta*, *75*(24), 7779–7791. https://doi.org/10.1016/j.gca.2011.10.011

Ketcham, R. A., Mora, A., & Parra, M. (2018). Deciphering exhumation and burial history with multi-sample down-well thermochronometric inverse modelling. *Basin Research*, *30*(S1), 48–64. https://doi.org/10.1111/bre.12207

Kissling, W. (1999). Modeling of cooling plutons in the Taupo volcanic zone, New Zealand. In *Proc. Twenty-fourth workshop on geothermal reservoir engineering* (pp. 25–27). Stanford University.

Kissling, W. M. (1995). Extending MULKOM to super-critical temperatures and pressures. In *Proceedings of the World Geothermal Congress*, (pp. 1687–1690).

Kissling, W. M., Ellis, S. E., McNamara, D. D., & Massiot, C. (2015). Modelling fluid flow through fractured rock: Examples using TVZ geothermal reservoirs. In *Paper presented at 37th New Zealand Geothermal Workshop*. Taupo.

Koshnaw, R., Stockli, D., & Schlunegger, F. (2019). Timing of the Arabia-Eurasia continental collision—Evidence from detrital zircon U-Pb geochronology of the red bed series strata of the northwest Zagros hinterland, Kurdistan region of Iraq. *Geology*, *47*(8), e471. https://doi.org/10.1130/G45499.1

Lis-Śledziona, A. (2019). Petrophysical rock typing and permeability prediction in tight sandstone reservoir. *Acta Geophysica*, *67*(6), 1895–1911. https://doi.org/10.1007/s11600-019-00348-5

Lotfi, M. (2001). *Geological map of Mahneshan, scale: 1:100,000*. Geological Survey of Iran.

Luijendijk, E. (2019). Beo v1.0: Numerical model of heat flow and low-temperature thermochronology in hydrothermal systems. *Geoscientific Model Development*, *12*(9), 4061–4073. https://doi.org/10.5194/gmd-12-4061-2019

Madanipour, S., Ehlers, T. A., Yassaghi, A., & Enkelmann, E. (2017). Accelerated middle Miocene exhumation of the Talesh mountains constrained by U-Th/He thermochronometry: Evidence for the Arabia-Eurasia collision in the NW Iranian Plateau. *Tectonics*, *36*(8), 1538–1561. https://doi.org/10.1002/2016TC004291

Manning, C. E., & Ingebritsen, S. E. (1999). Permeability of the continental crust: Implications of geothermal data and metamorphic systems. *Reviews of Geophysics*, *37*(1), 127–150. https://doi.org/10.1029/1998RG900002

McKenzie, D., & Priestley, K. (2008). The influence of lithospheric thickness variations on continental evolution. *Lithos*, *102*(1–2), 1–11. https://doi.org/10.1016/j.lithos.2007.05.005

McQuarrie, N., & van Hinsbergen, D. (2013). Retrodeforming the Arabia-Eurasia collision zone: Age of collision versus magnitude of continental subduction. *Geology*, *41*(3), 315–318. https://doi.org/10.1130/G33591.1

Meesters, A. G. C. A., & Dunai, T. J. (2005). A noniterative solution of the (U-Th)/He age equation. *Geochemistry, Geophys. Geosystems*, *6*(4), Q04002. https://doi.org/10.1029/2004GC000834

Mehrabi, B., Yardley, B. W. D., & Cann, J. R. (1999). Sediment-hosted disseminated gold at Zarshuran, NW Iran. *Mineralium Deposita*, *34*(7), 673–696. https://doi.org/10.1007/s001260050227

Moazzen, M., Hajialioghli, R., Moller, A., Droop, G. T. R., Oberhansli, R., Altenberger, U., & Jahangiri, A. (2013). Oligocene partial melting in the Takab metamorphic complex, NW Iran: Evidence from in situ U-Pb geochronology. *Journal of Sciences, Islamic Republic of Iran*, *24*(3), 217–228.

Moazzen, M., Oberhansli, R., Hajialioghli, R., Moller, A., Bousquet, R., Droop, G. T. R., & Jahangiri, A. (2009). Peak and post-peak P–T conditions and fluid composition for scapolite clinopyroxene–garnet calc-silicate rocks from the Takab area, NW Iran. *European Journal of Mineralogy*, *21*(14), 149–162. https://doi.org/10.1127/0935-1221/2009/0021-1887

Mohammadi, E., Vaziri, M. R., & Dastanpour, M. (2015). Biostratigraphy of the nummulitids and lepidocyclinids bearing Qom Formation based on larger benthic foraminifera (Sanandaj–Sirjan fore-arc basin and Central Iran back-arc basin, Iran). *Arabian Journal of Geosciences*, *8*(1), 403–423. https://doi.org/10.1007/s12517-013-1136-6

Morley, C., Kongwung, B., Julapour, A. A., Abdolghafourian, A., Hajian, M., Waples, D., et al. (2009). Structural development of the major late Cenozoic basin and transpressional belt in Central Iran: The Central Basin in the Qom-Saveh area. *Geosphere*, *5*(4), 325–362. https://doi.org/10.1130/GES00223.1

Mouthereau, F., Lacombe, O., & Verges, J. (2012). Building the Zagros collisional orogen: Timing, strain distribution and the dynamics of Arabia/Eurasia plate convergence. *Tectonophysics*, *532–535*, 27–60. https://doi.org/10.1016/j.tecto.2012.01.022

Murray, K. E., Braun, J., & Reiners, P. W. (2018). Toward robust interpretation of low-temperature thermochronometers in magmatic terranes. *Geochemistry, Geophysics, Geosystems*, *19*(10), 3739–3763. https://doi.org/10.1029/2018GC007595

Murray, K. E., Goddard, A. L. S., Wildman, M., & Wildman, M. (2022). Thermal history modeling techniques and interpretation strategies: Applications using HeFTy. *Geosphere*, *18*(5), 1–21. https://doi.org/10.1130/GES02500.1

Norton, D., & Taylor, H. P., Jr. (1979). Quantitative simulation of the hydrothermal systems of crystallizing magmas on the basis of transport theory and oxygen isotope data: An analysis of the Skaergaard intrusion. *Journal of Petrology*, *20*(3), 421–486. https://doi.org/10.1093/petrology/20.3.421

Nuriel, P., Weinberger, R., Clark, A. K., Hacker, B. R., & Craddock, J. (2017). The onset of Dead Sea transform based on calcite age-strain analysis. *Geology*, *45*(7), 587–590. https://doi.org/10.1130/G38903.1

O'Sullivan, P. B., & Parrish, R. R. (1995). The importance of apatite composition and single-grain ages when interpreting AFT data from plutonic rocks: A case study from the Coast Ranges, British Columbia. *Earth and Planetary Science Letters*, *132*(1–4), 213–224. https://doi.org/10.1016/0012-821x(95)00058-k

Paknia, M., Ballato, P., Heidarzadeh, G., Cifelli, F., Hassanzadeh, J., Vezzoli, G., et al. (2021). Neogene tectono-stratigraphic evolution of the intermontane Tarom basin: Insights into basin filling and plateau building processes along the northern margin of the Iranian Plateau (Arabia-Eurasia collision zone). *Tectonics*, *40*(3), e2020TC006254. https://doi.org/10.1029/2020TC006254

Paknia, M., Ballato, P., Heidarzadeh, G., Cifelli, F., Oskooi, B., Feinberg, J., et al. (2021). Middle-late Miocene normal faulting in the intermontane Tarom basin during the collisional deformation of the Arabia-Eurasia collision zone, NW Iran: A regional process or a local feature? *Journal of Asian Earth Sciences*, *217*, 104846. https://doi.org/10.1016/j.jseaes.2021.104846

Parmentier, E., & Schedl, A. (1981). Thermal aureoles of igneous intrusions: Some possible indications of hydrothermal convective cooling. *Geology*, *89*, 1–22. https://doi.org/10.1086/628561

Pauwels, H., Fouillac, C., & Fouillac, A. M. (1993). Chemistry and isotopes of deep geothermal saline fluids in the Upper Rhine Graben: Origin of compounds and water-rock interactions. *Geochimica et Cosmochimica Acta*, *57*(12), 2737–2749. https://doi.org/10.1016/0016-7037(93)90387-C

Pirouz, M., Jean-Philippe, A., Hassanzadeh, J., & Bahroudi, A. (2017). Early Neogene foreland of the Zagros, implications for the initial closure of the Neo-Tethys and kinematics of crustal shortening. *Earth and Planetary Science Letters*, *477*, 168–182. https://doi.org/10.1016/j.epsl.2017.07.046

Pruess, K. (1991). *TOUGH2 – A general-purpose numerical simulator for multiphase fluid and heatflow*, Report LBL-29400. Lawrence Berkeley Lab. https://doi.org/10.2172/5212064

Rabiee, A., Rossetti, F., Asahara, Y., Azizi, H., Lucci, F., Lustrino, M., & Nozaem, R. (2020). Long-lived, Eocene-Miocene stationary magmatism in NW Iran along a transform plate boundary. *Gondwana Research*, *85*, 237–262. https://doi.org/10.1016/j.gr.2020.03.014

Rabiee, A., Rossetti, F., Lucci, F., & Lustrino, M. (2022). Cenozoic porphyry and other hydrothermal ore deposits along the South Caucasus-west Iranian tectono-magmatic belt: A critical reappraisal of the controlling factors. *Lithos*, *430–431*, 106874. https://doi.org/10.1016/j.lithos.2022.106874

Reiners, P. W. (2009). Nonmonotonic thermal histories and contrasting kinetics of multiple thermochronometers. *Geochimica et Cosmochimica Acta*, *73*(12), 3612–3629. https://doi.org/10.1016/j.gca.2009.03.038

Reiners, P. W., & Farley, K. A. (2001). Influence of crystal size on apatite (U–Th)/He thermochronology: An example from the Bighorn Mountains, Wyoming. *Earth and Planetary Science Letters*, *188*(3–4), 413–420. https://doi.org/10.1016/S0012-821X(01)00341-7

Reiners, P. W., Farley, K. A., & Hickes, H. J. (2002). He diffusion and (U–Th)/He thermochronometry of zircon; initial results from Fish Canyon Tuff and Gold Butte. *Tectonophysics*, *349*(1–4), 297–308. https://doi.org/10.1016/S0040-1951(02)00058-6

Reiners, P. W., Spell, T. L., Nicolescu, S., & Zanetti, K. A. (2004). Zircon (U–Th)/He thermochronometry: He diffusion and comparisons with $^{40}Ar/^{39}Ar$ dating. *Geochimica et Cosmochimica Acta*, *68*(8), 1857–1887. https://doi.org/10.1016/j.gca.2009.03.038

Robert, A. M. M., Letouzey, J., Kavoosi, M. A., Sherkati, S., Müller, C., Vergés, J., & Aghabaei, A. (2014). Structural evolution of the Kopeh Dagh fold-and-thrust belt (NE Iran) and interactions with the south Caspian Sea Basin and Amu Darya Basin. *Marine and Petroleum Geology*, *57*, 68–87. https://doi.org/10.1016/j.marpetgeo.2014.05.002

Roshanak, R., Moore, F., Zarasvandi, A., Keshavarzi, B., & Gratzer, R. (2018). Stable isotope geochemistry and petrography of the Qorveh–Takab travertines in northwest Iran. *Australian Journal of Earth Sciences*, *111*(1), 64–74. https://doi.org/10.17738/ajes.2018.0005

Saki, A., Moazzen, M., & Oberhansli, R. (2012). Mineral chemistry and thermobarometry of the staurolite-chloritoid schists from Poshtuk, NW Iran. *Geological Magazine*, *149*(6), 1077–1088. https://doi.org/10.1017/S0016756812000209

Sánchez, F., Barrea, A., Dávila, F. M., & Mora, A. (2021). Fetkin-hydro, a new hermos-hydrological algorithm for low-temperature thermochronological modeling. *Geoscience Frontiers*, *12*(3), 101074. https://doi.org/10.1016/j.gsf.2020.09.005

Schmidt, J., Hacker, B., Ratschbacher, L., Stübner, K., Stearns, M., Kylander-Clark, A., et al. (2011). Cenozoic deep crust in the Pamir. *Earth and Planetary Science Letters*, *312*(3–4), 411–421. https://doi.org/10.1016/j.epsl.2011.10.034

Sengor, A. M. C., Tuysuz, O., Imren, C., Sakinc, M., Eyidogan, H., Gorur, G., et al. (2005). The North Anatolian fault: A new look. *Annual Review of Earth and Planetary Sciences*, *33*(1), 37–112. https://doi.org/10.1146/annurev.earth.32.101802.120415

Sepahi, A. A., Ghoreishvandi, H., Maanijou, M., Maruoka, T., & Vahidpour, H. (2020). Geochemical description and sulfur isotope data for Shahrak intrusive body and related Fe-mineralization (east Takab), NW Iran. *Island Arc*, *29*(1), e12367. https://doi.org/10.1111/iar.12367

Shafaii Moghadam, H., Griffin, W. L., Xian-Hua, L., Santos, J. F., Karsli, O., Stern, R. J., et al. (2017). Crustal evolution of NW Iran: Cadomian Arcs, Archean fragments and the Cenozoic magmatic flare-up. *Journal of Petrology*, *58*(11), 2143–2190. https://doi.org/10.1093/petrology/egy005

Shafaii Moghadam, H., Li, X. H., Stern, R. J., Ghorbani, G., & Bakhshizad, F. (2016). Zircon U–Pb ages and Hf–O isotopic composition of migmatites from the Zanjan-Takab complex, NW Iran: Constraints on partial melting of metasediments. *Lithos*, *240–243*, 34–48. https://doi.org/10.1016/j.lithos.2015.11.004

Shuster, D. L., Flowers, R. M., & Farley, K. A. (2006). The influence of natural radiation damage on helium diffusion kinetics in apatite. *Earth and Planetary Science Letters*, *249*(3–4), 148–161. https://doi.org/10.1016/j.epsl.2006.07.028

Stockli, D. F., Hassanzadeh, J., Stockli, L. D., Axen, G. J., Walker, J. D., & Dewane, T. J. (2004). Structural and geochronological evidence for Oligo-Miocene intra-arc low-angle detachment faulting in the Takab–Zanjan area NW Iran. In *Abstract, Programs Geological Society of America*, (Vol. 36, No. (5), p. 319).

Stöcklin, J. (1968). Structural history and tectonics of Iran: A review. *The American Association of Petroleum Geologists Bulletin*, *52*, 1229–1258. https://doi.org/10.1306/5D25C4A5-16C1-11D7-8645000102C1865D

Stübner, K., Ratschbacher, L., Rutte, D., Stanek, K., Minaev, V., Wiesinger, M., et al. (2013). The giant Shakhdara migmatitic gneiss dome, Pamir, India–Asia collision zone, I: Geometry and kinematics. *Tectonics*, *32*(5), 1404–1431. https://doi.org/10.1002/tect.20057

Tadayon, M., Rossetti, F., Zattin, M., Calzolari, G., Nozaem, R., Salvini, F., et al. (2018). The long-term evolution of the Doruneh Fault region (Central Iran): A key to understand the spatio-temporal tectonic evolution in the hinterland of the Zagros convergence zone. *Geological Journal*, *54*(3), 1454–1479. https://doi.org/10.1002/gj.3241

Tanaka, A., Yamano, M., Yano, Y., & Sasada, M. (2004). Geothermal gradient and heat flow data in and around Japan, Digital Geosci. Map DGMP-5. *Geological Survey of Japan*.

Teknik, V., & Ghods, A. (2017). Depth of magnetic basement in Iran based on fractal spectral analysis. *Geophysical Journal International*, *209*(3), 1878–1891. https://doi.org/10.1093/gji/ggx132

Tikoff, B., & Teyssier, C. (1994). Strain modeling of displacement-field partitioning in transpressional orogens. *Journal of Structural Geology*, *16*(11), 1575–1588. https://doi.org/10.1016/0191-8141(94)90034-5

Turcotte, D. L., & Schubert, G. (2002). *Geodynamics* (2nd ed., p. 456). Cambridge University.

Verdel, C., Wernicke, B. P., Hassanzadeh, J., & Guest, B. (2011). A Paleogene extensional arc flare-up in Iran. *Tectonics*, *30*(3), 1–19. https://doi.org/10.1029/2010TC002809

Verdel, C., Wernicke, B. P., Ramezani, J., Hassanzadeh, J., Renne, P. R., & Spell, T. L. (2007). Geology and thermochronology of Tertiary Cordille-ran-style metamorphic core complexes in the Saghand region of central Iran. *The Geological Society of America Bulletin*, *119*(7–8), 961–977. https://doi.org/10.1130/B26102.1

Vernant, P., Nilforoushan, F., Hatzfeld, D., Abbassi, M., Vigny, C., Masson, F., et al. (2004). Contemporary crustal deformation and plate kinematics in Middle East constrained by GPS measurements in Iran and northern Iran. *Geophysical Journal International*, *157*(1), 381–398. https://doi.org/10.1111/j.1365-246X.2004.02222.x

Wagner, G. A., & Van den haute, P. (1992). *Fission-track dating* (p. 287). Kluwer Academic Publishers, Enke-Verlag.

Willett, S. D., Herman, F., Fox, M., Stalder, N., Ehlers, T. A., Jiao, R., & Yang, R. (2021). Bias and error in modelling thermochronometric data: Resolving a potential increase in Plio-Pleistocene erosion rate. *Earth Surface Dynamics*, *9*(5), 1153–1221. https://doi.org/10.5194/esurf-9-1153-2021

Wolf, R. A., Farley, K. A. L., & Silver, T. (1996). Helium diffusion and low temperature thermochronometry of apatite. *Geochimica et Cosmochimica Acta*, *60*(21), 4231–4240. https://doi.org/10.1016/S0016-7037(96)00192-5

Wolfe, M. R., & Stockli, D. F. (2010). Zircon (U-Th)/He thermochronometry in the KTB drill hole, Germany, and its implications for bulk He diffusion in Zircon, Earth Planet. *Science Letter*, *295*(1–2), 69–82. https://doi.org/10.1016/j.epsl.2010.03.025

Zhou, R., Schoenbohm, L. M., Sobel, E. R., Davis, D. W., & Glodny, J. (2017). New constraints on orogenic models of the southern Central Andean Plateau: Cenozoic basin evolution and bedrock exhumation. *The Geological Society of America Bulletin*, *129*(1–2), 152–170. https://doi.org/10.1130/B31384.1

Zhu, J., Hu, K., Lu, X., Huang, X., Liu, K., & Wu, X. (2015). A review of geothermal energy resources, development, and applications in China: Current status and prospects. *Energy*, *93*(12), 466–483. https://doi.org/10.1016/j.energy.2015.08.098

References From the Supporting Information

Bhandari, N., Bhat, S. G., Lal, D., Rajagopalan, G., Tamhane, A. S., & Venkatavaradan, V. S. (1971). Fission fragment tracks in apatite: Recordable track lengths. *Earth and Planetary Science Letters*, *13*(1), 191–199. https://doi.org/10.1016/0012-821X(71)90123-3

Dunkl, I. (2002). TRACKKEY: A windows program for calculation and graphical presentation of fission track data. *Computers and Geosciences*, *28*(1), 3–12. https://doi.org/10.1016/S0098-3004(01)00024-3

Farley, F. W., Soriano, P., Steffen, L. S., & Dymecki, S. M. (2000). *Widespread recombinase expression using FLPeR (Flipper) mice* (Vol. 28, pp. 106–110). Genesis. https://doi.org/10.1002/1526-968X(200011/12)28:3/4%3C106::AID-GENE30%3E3.0.CO;2-T

Galbraith, R. F. (1981). On statistical models for fission track counts. *Mathematical Geology*, *13*(6), 471–478. https://doi.org/10.1007/BF01034498

Gegenhuber, N., & Schon, J. (2014). Thermal conductivity estimation from elastic-wave velocity-application of a petrographic-coded model. *Petrophysics-The SPWLA Journal of Formation Evaluation and Reservoir Description*, *55*(01), 51–56.

Lange, R. A., Cashman, K. V., & Navrotsky, A. (1994). Direct measurements of latent heat during crystallization and melting of a ugandite and an olivine basalt. *Contributions to Mineralogy and Petrology*, *118*(2), 169–181. https://doi.org/10.1007/BF01052867

Miao, S. Q., Li, H. P., & Chen, G. (2014). Temperature dependence of thermal diffusivity, specific heat capacity, and thermal conductivity for several types of rocks. *Journal of Thermal Analysis and Calorimetry*, *115*(2), 1057–1063. https://doi.org/10.1007/s10973-013-3427-2

Namur, O., Abily, B., Boudreau, A. E., Blanchette, F., Bush, J. W., Ceuleneer, G., et al. (2015). Igneous layering in basaltic magma chambers. In *Layered intrusions* (pp. 75–152). Springer. https://doi.org/10.1007/978-94-017-9652-1_2

Seipold, U., & Huenges, E. (1998). Thermal properties of gneisses and amphibolites—High pressure and high temperature investigations of KTB-rock samples. *Tectonophysics*, *291*(1–4), 173–178. https://doi.org/10.1016/S0040-1951(98)00038-9